MANUFACTURING AND CHARACTERIZATION OF PEROVSKITE THIN FILMS USING NOVEL METHODS

A Thesis Submitted to the Graduate School of Engineering and Sciences of İzmir Institute of Technology in Partial Fulfillment of the Requirements for the Degree of

MASTER OF SCIENCE

in Photonics Science and Engineering

by

Ozan BIYIKLI

July 2020

İZMİR

ACKNOWLEDGMENTS

Firstly, I would like to thank my family who always supported me in this challenging process.

I would like to thank my supervisor Dr. Emre SARI, who gave me the responsibility of a new and novel system, which gave me great experience and knowledge.

I want to thank the interns and my friends at Photonic Department for their valuable assistance.

I would like to thank Dr. Özgenç EBİL and Dr. Evren MUTLUGÜN, who are the committee members of my thesis, for their participation and valuable comments.

ABSTRACT

MANUFACTURING AND CHARACTERIZATION OF PEROVSKITE THIN FILMS USING NOVEL METHODS

Perovskite photovoltaics is a promising technology due to its low-cost fabrication and high efficiency. Since their first demonstration in 2009, efficiencies of perovskite solar cells (PSCs) increased unprecedently fast from 3.81% to 25.2% in 10 years. The most common method for the deposition of the absorber layer of the perovskite solar cells is the spin-coating method, which is not a scalable method, and this method is an obstacle to their commercialization. Efficiencies obtained with scalable methods are currently lower than that of the spin-coating method.

In this thesis, among the scalable deposition methods, a novel ultrasonic spray-coating was used by adding antisolvent vapor to the system. The antisolvent quenching technique, that is commonly used to improve the crystalline quality of the film by spin-coating was successfully adapted for ultrasonic spray coating.

The interaction between diethyl ether (DE) vapor, which is used as an antisolvent, and $MAPb(I_{(3-x)}Br_x)_3$ precursor solution (where the solvent is DMF:DMSO, 4:1) was utilized to improve the crystalline quality of the perovskite film. As a result of this interaction, the intermediate phase was observed. The transition to the intermediate phase is supported by data from characterization methods such as optical microscopy, scanning electron microscopy (SEM), X-Ray diffraction (XRD), and current-voltage measurement.

Furthermore, n-i-p devices with the $FTO/c\text{-}TiO_2/m\text{-}TiO_2/MAPb(I_{(1-x)}Br_x)_3/Spiro\text{-}OMeTAD$ architecture were produced with different antisolvent vapors and their efficiencies was compared. It was observed that devices using DE vapor reach higher efficiencies than devices without any antisolvent vapor.

Keywords: Perovskite, Solar Cell, Antisolvent, Spray-Coating.

ÖZET

ÖZGÜN YÖNTEMLER İLE PEROVSKİT İNCE FİLMLERİN İMALATI VE KARAKTERİZASYONU

Perovskit fotovoltaikler düşük maliyetli üretimi ve yüksek verimlilikleri nedeniyle umut verici bir teknolojidir. 2009'daki ilk gösterimlerinden bu yana perovskite güneş pillerinin verimliliği 10 yılda %3.81'den %25.2'ye görülmemiş bir hızla ulaşmıştır. Perovskit güneş pillerinin emici tabakasının biriktirilmesi için kullanılan en yaygın yöntem dönel kaplamadır. Ölçeklenebilir bir yöntem olmayan dönel kaplama ile üretilen perovskit güneş pilleri ticarileşememektedir.

Bu tezde ölçeklenebilir bir metot olan ultrasonik sprey ile kaplama yöntemi, sisteme antisolvent buharı dahil edilerek kullanılmıştır. Dönel kaplama ile perovskit ince filmlerdeki kristal kalitesini artırmak amacıyla kullanılan antisolvent sönümleme tekniği ultrasonik sprey kaplama ile başarıya ulaşmıştır.

Antisolvent olarak kullanılan dietil eter (DE) buharı ve hacmen 4:1 oranındaki DMF:DMSO solventlerinin içinde bulunan $MAPb(I_{(1-x)}Br_x)_3$ öncül solüsyonunun etkileşimi gerçekleştirilmiştir. Bu etkileşim sonucunda ara faz gözlemlenmiştir. Ara faza geçiş, optik mikroskopi, tarayıcı elektron mikroskopisi (SEM), X-Işını Kırınımı (XRD) ve akım- gerilim ölçümleri ile karakterize edilmiş ve bu karakterizasyon yöntemlerinden elde edilen verilerle desteklenmiştir.

FTO/c-TiO$_2$/m-TiO$_2$/$MAPb(I_{(1-x)}Br_x)_3$/Spiro-OMeTAD mimarisine sahip n-i-p cihazlar farklı antisolvent buharlarıyla üretilmiş ve verimleri kendi aralarında karşılaştırılmıştır. DE buharı uygulanan cihazların herhangi bir antisolvent buharı uygulanmayan cihazlara nazaran daha yüksek verimlere ulaştığı görülmüştür.

Anahtar Kelimeler: Perovskit, Güneş Pili, Antisolvent, Sprey Kaplama.

TABLE OF CONTENTS

LIST OF TABLES

LIST OF FIGURES

LIST OF SYMBOLS

Symbol	Meaning
E_g	Bandgap energy
E_c	The minimum point of the conduction band
E_v	The maximum point of the valance band
E_F	Fermi Level
I_L	Photo-current
I_{SC}	Short-circuit current
V_{OC}	Open-circuit voltage
δ-phase	Yellow perovskite phase
α-phase	Black perovskite phase

LIST OF ABBREVATIONS

Abbrevation	Meaning
PV	Photovoltaic
PSC	Perovskite Solar Cell
PCE	Power Conversion Efficiency
CB	Conduction Band
VB	Valance Band
FF	Fill Factor
XRD	X-Ray Diffraction
SEM	Scanning Electron Microscopy
ETL	Electron Transport Layer
HTL	Hole Transport Layer
MA	Methylammonium
FA	Formamidinium
DMF	Dimethylformamide
DMSO	Dimethyl Sulfoxide
FTO	Fluorine-Doped Tin Oxide
DE	Diethyl Ether
TL	Toluene

CHAPTER 1

INTRODUCTION

1.1. Renewable Energy

For many years, mankind has unconsciously consumed the finite earth resources and this unconscious consumption has started to damage the environment and living creatures in time. The excessive use of non-renewable energy sources has major damages, such as carbon dioxide (CO_2) emission. This emission causes increase in the greenhouse effect in the atmosphere and the earth starts to get warmer. As a result, climate change occurs. In 2013, Intergovernmental Panel on Climate Change (IPCC) reported that the global average surface temperature increased by 0.85 °C between 1885- 2012 (Ipcc 2013). CO_2 emission is an important factor leading to global warming.

The biggest reason for CO_2 emission is the combustion of fossil fuels (coal, natural gas, oil). The burning of fossil fuels has 82% percent of CO_2 emission over the last half-century. Between 2009- 2018, the percentage of CO_2 emission from the combustion of fossil fuels increases and it becomes 86% (Friedlingstein et al. 2019a). In this time interval, 42% of fossil CO_2 emissions were from coal. Oil and natural gas followed coal with 34% and 19% percentages, respectively. Cement and other small sources had the remaining percent (Peters et al. 2020).
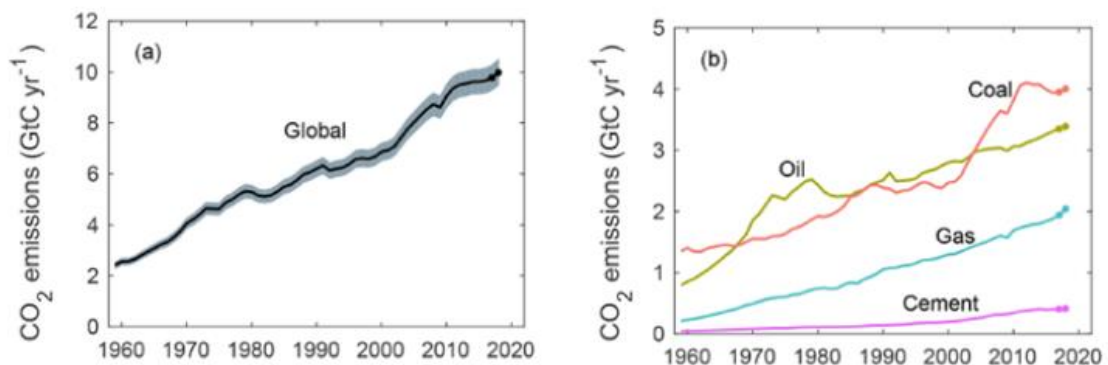
Figure 1. 1 (a) Globally, CO_2 emission from fossils, shaded gray represent uncertainty (±5%), black dots illustrate British Petroleum (BP) energy statistic

estimations, (b) CO_2 emission due to burning of fossils by fuel type, the dots indicate estimated from BP energy statistics for 2017-2018. Values are in terms of gigatonnes of carbon per year (Source: Friedlingstein et al. 2019b).

One solution would be to turn to alternative energy sources that have low or no environmental damage. Renewable energy sources have become a promising alternative energy source. It is obtained from natural sources that can renovate itself constantly. Solar energy, wind energy, geothermal energy, biomass, hydroelectric energy, hydrogen, ocean thermal energy, and ocean mechanical energy are types of renewable energy.

Renewable energy has made a great leap in electricity production in the last 10 years. It grew by an average of 16.4% from 2007 to 2017. Among the renewable energy types, wind energy (20.8%) and solar energy (50.2%) show the greatest improvement (BPSTATS 2019). The distribution of electricity generation in 2018 by resources is shown in Fig 1.2.
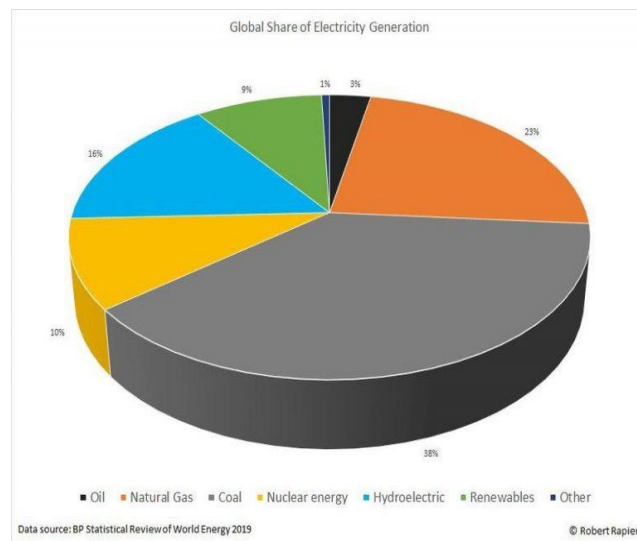
Figure 1. 2 Global Share of Electricity Generation in 2018
(Source: Rapier 2019).

1.2. Solar Energy

The sun is a vital energy source for the World in terms of sustainability, clean energy, and inexhaustibleness and it is an alternative source to fossil fuels with these features. Solar power has been used for many years to obtain electricity and thermal energy. In 1897, Frank Shuman run a motor with steam which is produced by heating a

liquid chemical that has a lower boiling point than water's (Smith and Taylor 2008). Photovoltaics (PV) is the technology to transform solar radiation into electricity. It is based on the photovoltaic effect, which is defined as the formation of voltage due to solar radiation that is falling on material, is discovered by Henri Becquerel in 1939 (Goetzberger and Hoffmann 2005).
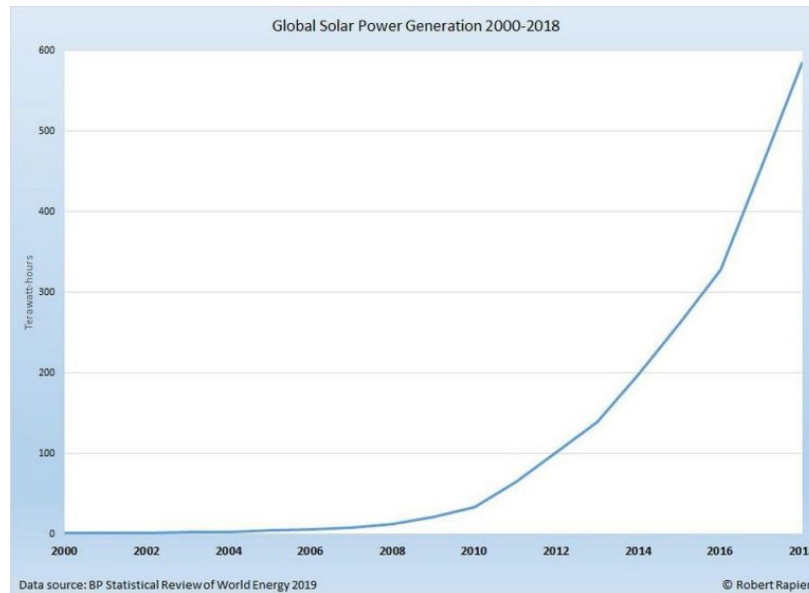
Figure 1. 3 Global Solar Power Generation 2000-2018
(Source: Rapier 2019).

As in Figure 1. 3, solar power generation is developing, constantly. The efficiency of photovoltaic power generation from the sun increases thanks to the developing technology including improvements in existing technologies and new emerging technologies. Considering the technological developments, the interest in solar energy is expected to rise further. This is a pleasing improvement for humanity.

1.3. Thesis Motivation

Perovskite Solar Cells (PSCs) have become a center of interest in the world of science with the high efficiency they have achieved in a short time. A scalable deposition technique should be used, in order to commercialize of perovskite solar cells successfully. Spray deposition is one of these scalable techniques. The antisolvent quenching method, which is used to improve crystallization quality, was used with spray deposition in this

thesis. It is desired that the antisolvent, which comes as vapor, to interact with the perovskite solution droplets. This interaction and its results are examined in this thesis.

1.4. Thesis Overview

In Chapter 2, perovskite solar cells will be introduced after the physics of solar cells are discussed in detail. Deposition methods and antisolvent quenching method will be explained and the qualified studies on PSCs will be summarized.

In Chapter 3, our novel ultrasonic spray coating system with antisolvent vapor will be introduced. Detailed information will be given on how the system works.

In Chapter 4, the production of PSCs will be explained step by step and the characterization methods used in this thesis will be introduced.

In Chapter 5, the results from the experiments will be explained and discussed. Then, how the system can be improved will be discussed based on the results we have.

In Chapter 6, the conclusions drawn from the thesis will be summarized.

CHAPTER 2

BACKGROUND THEORY

2.1. Solar Cell

Solar cells transform directly sunlight to electricity with good efficiency as a result of the photovoltaic effect. The first solar cell, which was based on silicon, was discovered at Bell Laboratories in 1954, and it had 6% efficiency approximately (Chapin, Fuller, and Pearson 1954). When the sunlight, in the form of photons, contact with the surface of the material, these photons are absorbed by the material. In this way, electron and hole, which are required to produce electricity, is generated. This is the basic working principle of solar cells, however some concepts need to be explained in depth for examining the subject.

2.1.1. Band Structure of Semiconductors

Solid-state materials are divided into three groups as insulators, conductors, and semiconductors. The conductivity of the insulators is low and the conductivity of the conductors is high. Semiconductors can conduct current when certain conditions are met. These conditions are illumination, temperature, magnetic field, and impurity atoms.

Semiconductors have a crystal structure and atoms are in a fixed position in the crystal structure. The arrangement of atoms in the crystal structure is called a lattice. A lattice is represented by a unit cell that repeats through the crystal and builds the lattice (Fonash 2010).

The valence electrons of atoms in the crystal structure are connected by covalent bonding as shown in Figure 2. 1. These bonds can break due to thermal vibration at high temperatures. When the bond breaks, an electron is free and leaves a "hole" behind it. Another neighbor valence electron can fill the hole and this hole shifts eventually. A hole is an imaginary particle similar to an electron and carries a positive charge and moves under the applied electric field (Sze 2002).
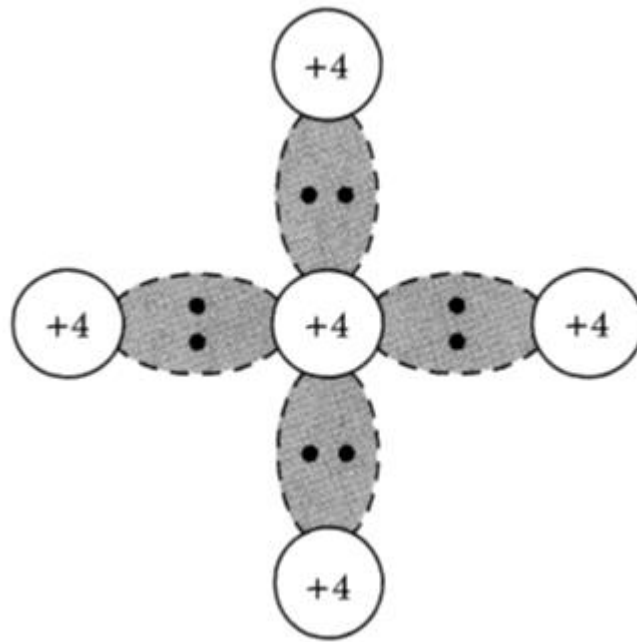
Figure 2. 1 The representation of covalent bonding between atoms which have four
valence electrons (Source: Sze 2002).

When two identical atoms with the same energy level approach each other, atomic interaction occurs and their energy levels separate into two levels. To form a crystal structure, N atoms get together and N energy levels are created. These energy levels are close to each other due to atomic interaction. This formation is a continuous energy state and it is called a band. When the distance between atoms decreases, even more, this band is divided into two bands (Sze 1985). The two newly formed bands are separated from each other by a region which is known as the forbidden gap or bandgap (E_g). The band occupied by electrons is called the valence band, and the unoccupied band is called the conduction band.
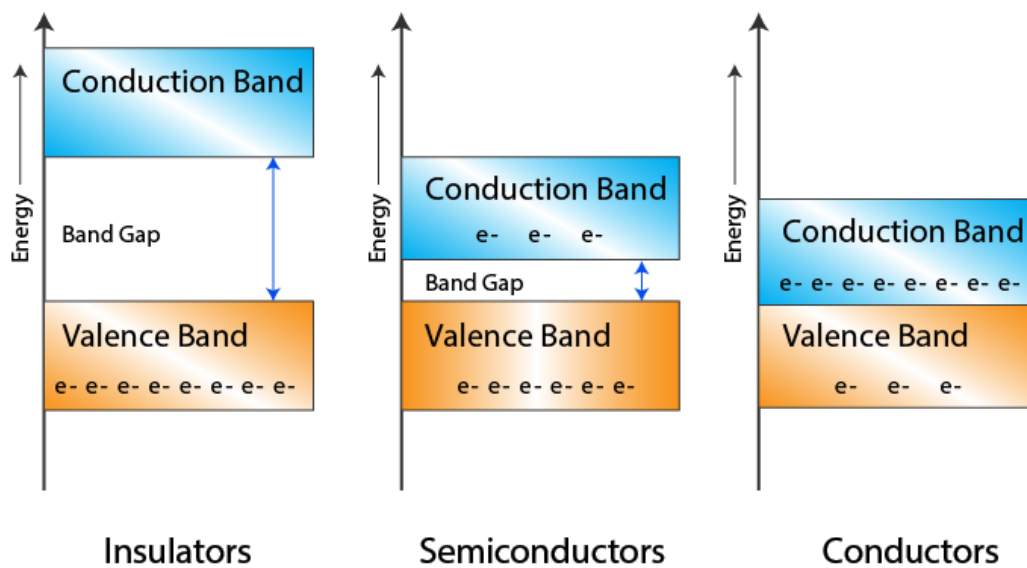
Figure 2. 2 Band structure of insulators, semiconductors, and conductors. The bandgap is calculated by subtracting the maximum point of the valence band (E_v) from the minimum point of the conduction band (E_c), that is, $E_g = E_c - E_v$. If the E_g is higher than 3 eV, the solid is an insulator. If the bandgap energy is between 0.5 eV and 3 eV, it is a semiconductor and if the E_g is lower than 0.5 eV, it is called a conductor (Source: Nelson 2003).

In isolators, valence electrons are closely connected with other atoms. It is difficult to break this bond. Therefore, there is no free electron to participate in electrical conduction. The forbidden gap energy of isolators is much higher than that of semiconductors. The valence bond is completely occupied by electrons, and the conduction band is entirely empty. As a result, isolators cannot conduct electricity.

For conductors, there is no bandgap between the conduction band and the valence band. Therefore, valence electrons easily pass from valence band to conduction band. Consequently, conductors always conduct electricity.

As covalent bonds between valence electrons of semiconductors are not stronger than that of isolators, these bonds can break under some conditions such as thermal vibration. As bandgap energy is low according to that of isolators, electrons can pass from valence band to conduction band. Under the applied electric field, holes in the valence band and electrons in the conduction band gain kinetic energy and they can conduct

electricity. The semiconductors can be conductor or isolator, conditionally. These properties make semiconductors unique.
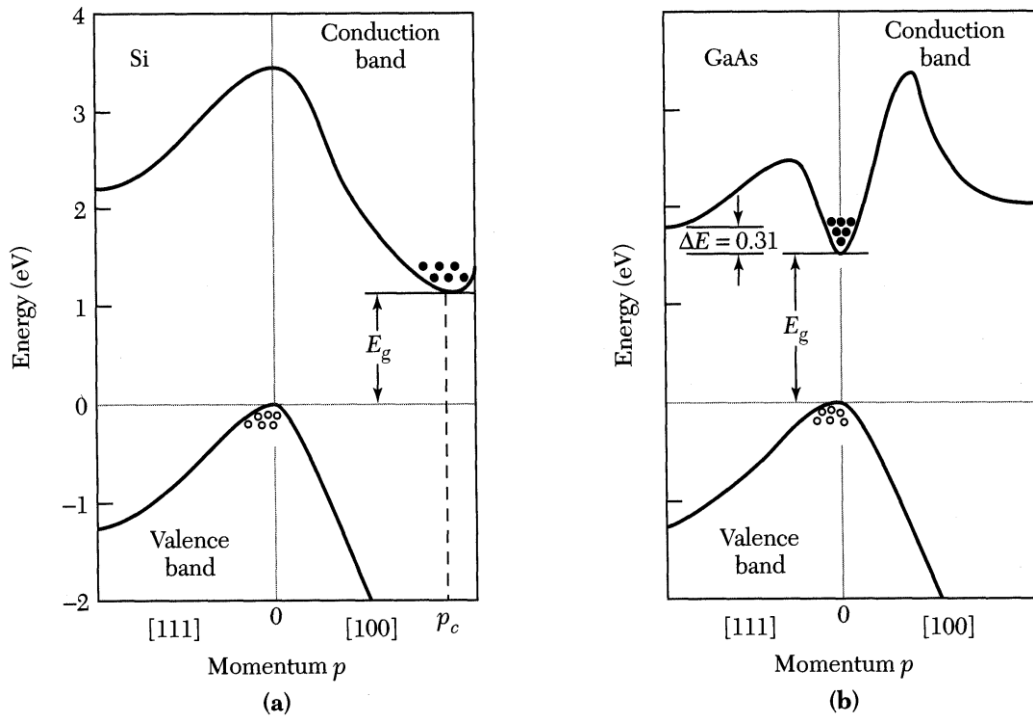
Figure 2. 3 Band structure of (a) silicon and (b) gallium arsenide. Dots show electrons and circles show holes (Source: Sze 2002).

The representation of the band structures of the semiconductors is more complicated than Figure 2. 2. The reason for this is crystal momentum (k-vector). If the top of the valence band and the bottom of the conduction band are in the same alignment, that is, p=0, it is called direct semiconductor such as GaAs which is known as an efficient solar cell. On the contrary, they are not in the same lineage, that is p≠0, it is called indirect semiconductor such as silicon. In electron transition from the valence band to the conduction band, it is not necessary to have an energy that will only pass E_g, and a change in crystal momentum is required.

Semiconductors with low impurities are called intrinsic semiconductors. In intrinsic semiconductors, Fermi Level (E_F), which is an energy state the probability of being occupied by electrons in half, is in the middle of the bandgap. The possibility of occupation of the energy state by an electron with E energy is given by the Fermi Dirac distribution function as given in Eqn. 2. 1:

$$f(E) = \frac{1}{\exp\left(\frac{(E - E_F)}{k_b T}\right)} \tag{2.1}$$

Where T is the temperature and k_b is the Boltzmann constant (Kittel 2004).

If a semiconductor is doped with impurities (dopants), it is called extrinsic semiconductor and formed intrinsic energy levels.
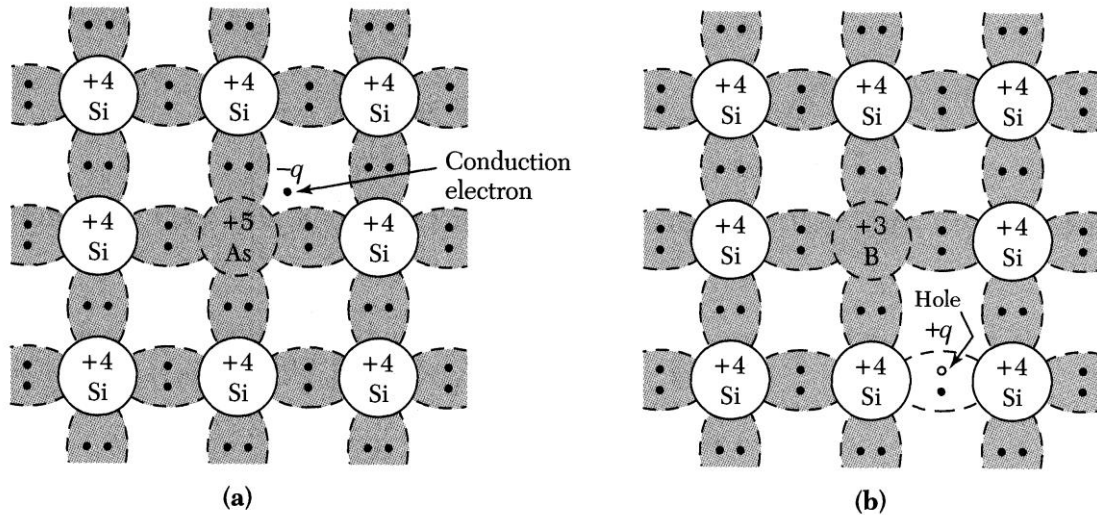
Figure 2. 4 Demonstration of bonds of n-type and p-type materials (a) Silicon doped with arsenic (b) Silicon doped with boron (Source: Sze 2002).

As shown in Figure 2.4 (a), a silicon atom with 4 valence electrons has been replaced by an Arsenic (As) atom with 5 valence electrons. When 4 electrons of the As atom form covalent bonds with those of the Si atom, an electron remains outside. This electron is donated to the conduction band by As. Silicon becomes n-type due to additional negative charge and arsenic becomes a donor. For Figure 2.4. (b), a silicon atom with 4 valence electrons is altered a boron atom with 3 valence electrons. To form 4 covalent bonds around the boron atom, the electron from other atoms is accepted by boron. The incoming electron leaves a hole in the valence band. Since an additional hole is formed, silicon becomes p-type and boron becomes an acceptor.

In intrinsic semiconductors, intrinsic Fermi level and Fermi level are equal ($E_i = E_F$). For extrinsic semiconductors, if the donor concentration is high, the Fermi level approaches the conduction band. Similarly, if there is high acceptor concentration, Fermi level shifts towards the valence band.

9
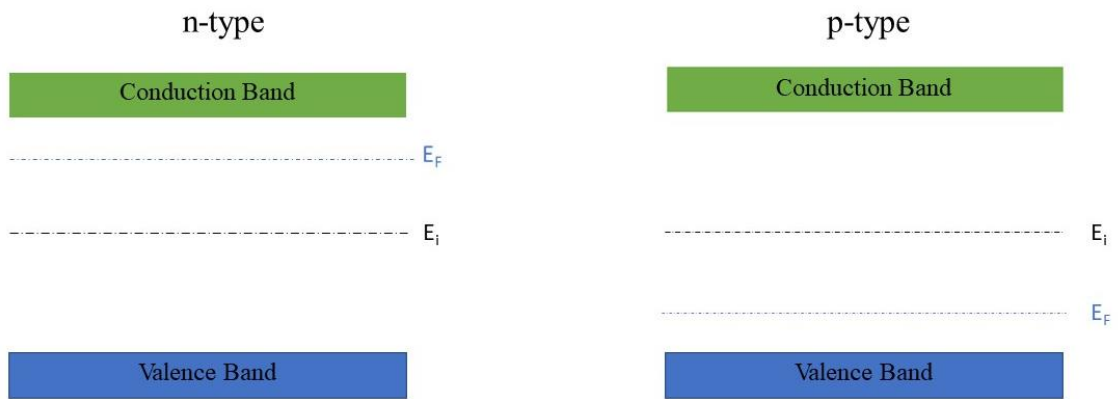
Figure 2. 5 The illustration of Fermi level shift for n-type and p-type materials.

2.1.2. p-n Junction

If p-region and n-region combine, they form a p-n junction for a single crystal semiconductor. By the combining of these regions, holes on the p-region begin to diffuse to the n-region and electrons on the n-region to the p-region, it is called diffusion current. Thus, a negative area near the p-region and a positive area near the n-region is formed and an electric field is created from diffused positive charges to diffused negative charges as shown in Figure 2. 6. The direction of the electric field is opposite to the diffusion current for each type of carrier.
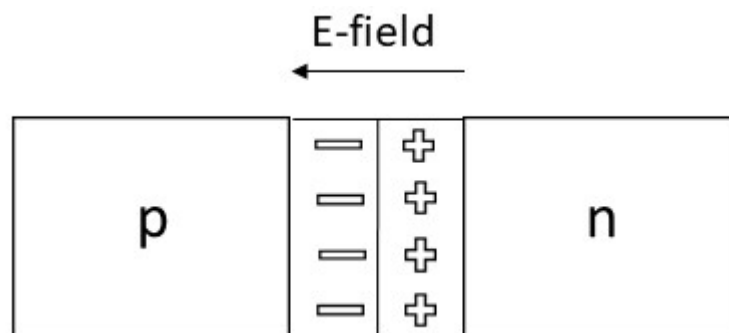
Figure 2. 6 The simple illustration of the electric field direction of p-n junction.

Under the applied electric field, electrons are drifted opposite direction of the electric field. On the contrary, holes are drifted towards the direction of the electric field. It is called drift current. Hole drift current flows from n-region to p-region and hole

diffusion current flows from p-region to n-region. Similarly, electron drift current flows from p-region to n-region and electron diffusion current flows in the opposite direction.

At thermal equilibrium, drift current equals to diffusion current, that is, net current flow is zero in a region of the p-n junction, this region is called depletion region or space charge region which has no mobile carrier (Fig 2.7). The potential difference in the neutral region between the p-side and the n-side is called built-in potential and is indicated by V_{bi}. This potential maintains the balance between carriers in the n-side and p-side (Neamen 2006). Fermi level is constant at thermal equilibrium.
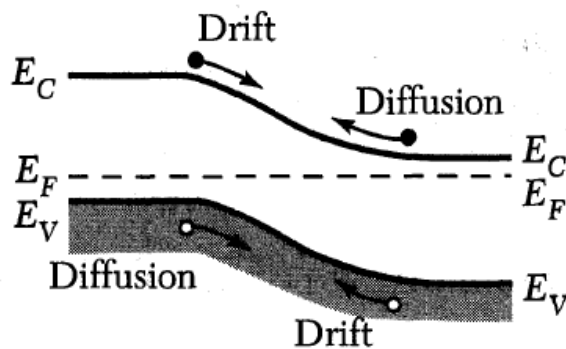
Figure 2. 7 The directions of drift current and diffusion current. Dots show electrons, circles show holes (Source: Sze 2002).

If the positive voltage is given from p-side to n-side, this is called forward bias. Under the forward bias, the applied voltage decreases potential in the depletion region. Therefore, the drift current decreases and diffusion current becomes dominant. Hole diffusion from p-side to n-side and electron diffusion from n-side to p-side enhance. In this way, holes are injected to the n-side, and electrons are injected to p-side. It is called minority carrier injection. The reason why it is called "minority" is that the type of carrier sent is a minority in the region. This process makes the depletion region narrower compared to thermal equilibrium case.

While the positive voltage is applied from the n-side to p-side, which is called reverse bias, the depletion region will be wider than that of the p-n junction without external biased. In this process, the potential in the depletion region increases under reverse bias. The diffusion current reduces and drift current becomes dominant and majority carrier injection takes place, that is, the holes generated in the n-side move to the p-side and the electron generated in the p-side pass to the n-side.

2.1.3. p-n Junction Solar Cell

Apart from forward biasing and reverse biasing, another carrier injection method is optical excitation, that is, sending photons to the p-n junction. If the energy of the photon is higher than that of bandgap, it is absorbed by the semiconductor. Electrons that gain the energy of photons in the valance band move to the conduction band. The electrons in the p-side move to the n-side due to the electric field in the junction. Electron-hole pairs (excitons) are generated in the depletion region. Then, the electric field in the depletion region drifts electron and holes out of the region and potential difference is created between the n-side and p-side. If these sides are connected with an external circuit, electrons begin to move to the p-side and the current is formed which is called photo-current (I_L). There is another current in the opposite direction of the photocurrent, this is called dark current which is formed due to random electrons and holes remaining in the space charge region. This is the reason that the weak current passes through the solar cell in the dark condition.

2.1.4 Equivalent Circuit of Solar Cells
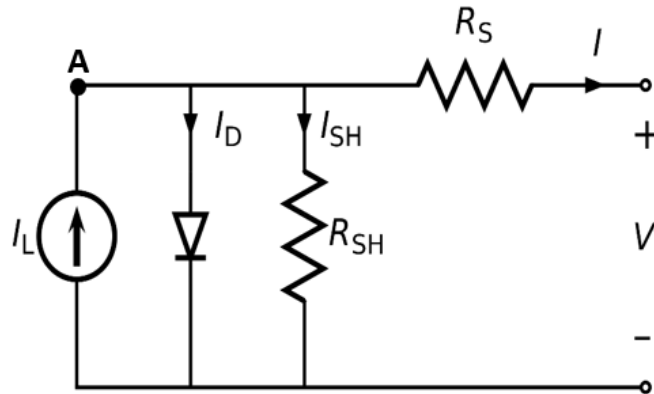
Figure 2. 8 The equivalent circuit of a solar cell under the illumination.

To find the current of the junction (I), Kirchhoff's current law is used in the "A" node:

$$I = I_L - I_D - I_{SH} \tag{2.2}$$

Where I_L is the photo-current of the solar cell, I_D is the diode current, and I_{SH} is the shunt current.

Since parallel voltages equal to each other, the voltage of the diode can be written as:

$$V_D = I_{SH}R_{SH} \tag{2.3}$$

Then, diode voltage is written in output voltage as follows

$$V_D = V + IR_S \tag{2.4}$$

The diode current can be described by Shockley equation for an ideal diode:

$$I_D = I_0 \left[\exp\left(\frac{V + IR_S}{nV_T}\right) - 1 \right] \tag{2.5}$$

Here, I_0 is the saturation voltage, n is the ideality factor of a diode, R_S is the series resistance, and V_T is the thermal voltage. The ideality factor must be 1 for ideal diodes. The condition of n=1 means no recombination along the junction. This case is theoretical; in reality, this value is between 1 and 2.

Then, V_T can be written as

$$V_T = \frac{k_B T}{q} \tag{2.6}$$

Where q is the elementary charge, k_B is the Boltzmann constant and T is the temperature.

By combining these equations, the output current can be written as

$$I = I_L - I_0 \left[exp\left(\frac{q(V + IR_S)}{k_B T}\right) - 1 \right] - \frac{V + IR_S}{R_{SH}} \tag{2.7}$$

2.1.5 I-V Characteristics of Solar Cell

The I-V characteristic of solar cells is utilized to calculate the efficiency of the device and to understand its electrical properties. In order to interpret the I-V characteristic, it is necessary to explain some terms.

Open circuit voltage (V_{OC}) is the measured maximum voltage between two terminals of the circuit when there is no current. When the voltage in the device is zero, the maximum current occurs, it is called short circuit voltage (I_{SC}).

13
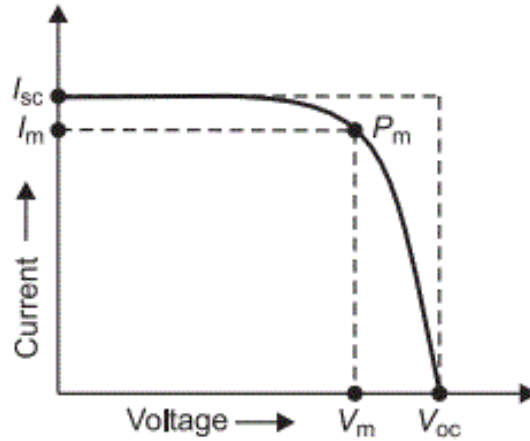
Figure 2. 9 I-V characteristics of a solar cell. I_m is the current at the maximum power, V_m is the voltage at maximum power, and P_m is the maximum power point.

Fill Factor (FF) is a significant parameter in determining the quality of a solar cell. The calculation of FF is as follows:

$$FF = \frac{I_m V_m}{I_{sc} V_{oc}} \tag{2.8}$$

FF should be close to 100% for an ideal solar cell, but it is impossible because of the existence of R_S and R_{SH} in real. Increasing the RS will decrease the maximum power point (P_{mp}) and therefore the fill factor. If the R_{SH} decreases, FF also decreases.
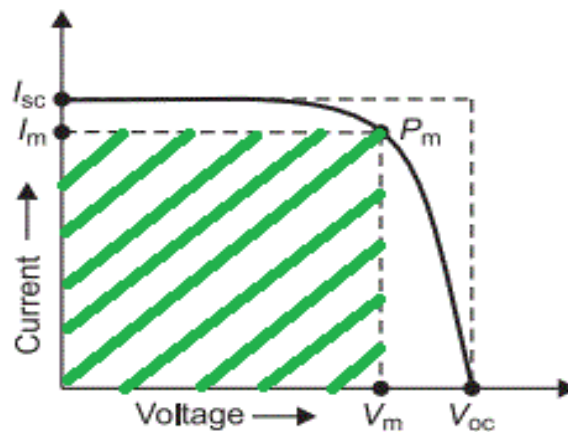
Figure 2. 10 Fill Factor of a solar cell. FF is calculated by dividing the area of the green striped rectangle by the area of the large rectangle.

14

2.1.6 Efficiency Measurement in Solar Cells

The light coming from the sun penetrates the solar cell with a wide spectrum range. The spectrum varies depending on weather conditions, time, location, and season. Hence, standard spectra are needed to investigate and develop solar cells, scientifically. Besides, standardization allows us to compare solar cell performance with other devices, since all of the solar cells are exposed the same spectra.

The effect of the atmosphere on the sunlight coming to the earth's surface is defined by air mass (AM). Air mass zero (AM0) condition relates to spectra outside the atmosphere. Air mass 1.5 (AM 1.5) condition represents the coming of sunlight to the earth at a zenith angle of 48.2° corresponds to an incident power is 1000 W/m^2. The efficiency of a solar cell is measured under AM 1.5 condition (Nelson 2003; Sze 2002).
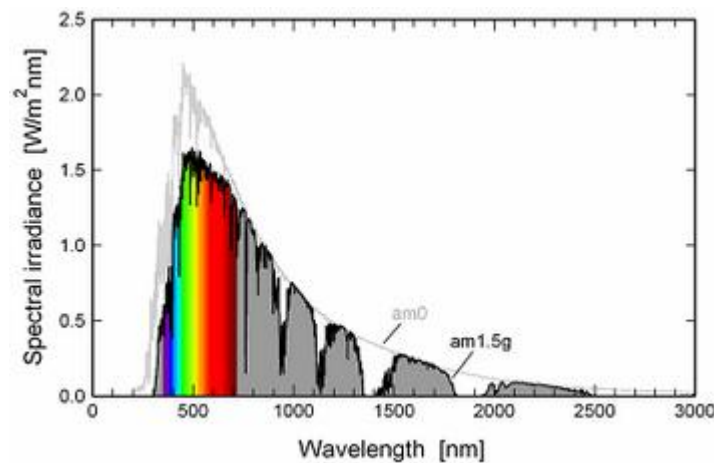
Figure 2. 11 Spectral irradiance of AM0 (Air Mass zero) and AM1.5g (Air Mass 1.5 global).

The comparison of the performance of solar cells is performed by calculating power conversion efficiency (PCE) below:

$$\eta = \frac{P_m}{P_{inc}} = \frac{I_m V_m}{P_{inc}} \tag{2.9}$$

Here, P_m is the maximum power point, I_m is the current at maximum power, and V_m is the voltage at the maximum point.

If equations (2.8) and (2.9) is combined, the new equation would be:

$$\eta = \frac{I_{SC}V_{OC}FF}{P_{inc}} \qquad (2.10)$$

Here, ɳ is the power conversion efficiency (PCE) and P_{inc} is the incoming power density of light (1000 W/m^2). Based on this equation, the highest efficiency is obtained by maximizing fill factor, open-circuit voltage, and short circuit current.

Another important efficiency measurement is the quantum efficiency, which is divided into two as external quantum efficiency (EQE) and internal quantum efficiency (IQE). Quantum efficiency is defined as the ratio of the photons coming to the device to the number of electrons, which are generated because of incident photons, in the circuit. EQE measures the transform of photons, which fall on the solar cell, into electrons that can be useable in electricity generation. On the contrary, IQE measures the conversion of absorbed photons by the device into usable electrons. Quantum efficiency is different from PCE in this aspect, since it does not contain information about the power of incoming light.

2.1.6 The Shockley-Quiesser Limit

Physical laws limit the maximum theoretical efficiency of single-junction solar cells. This limitation is known as Shockley-Quiesser Limit which is calculated by William Shockley and Hans-Joachim Queisser in 1961. According to this calculation, the maximum limit was approximately 33% at 1.4-1.5 eV (Shockley and Queisser 1961). The remaining percentage belongs to losses. Essentially, there are four losses sources.
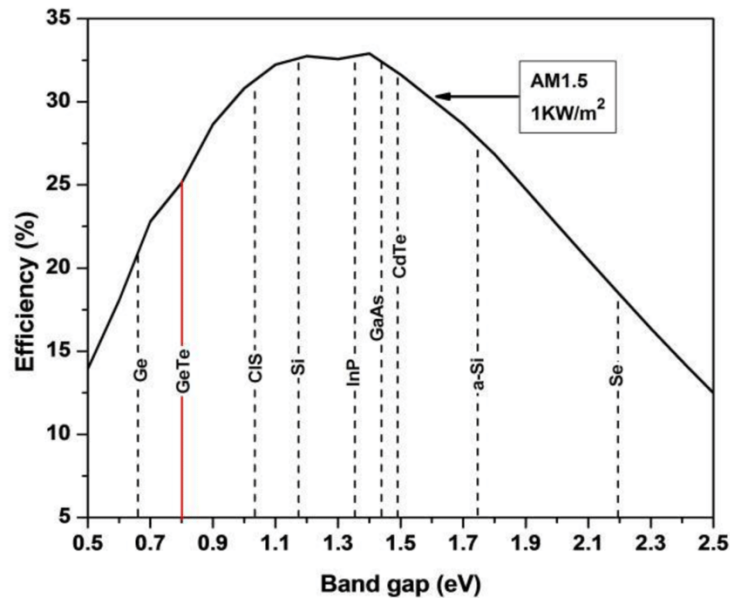
Figure 2. 12 Shockley-Quiesser Limit

(Source: Noman, Abden, and Islam 2018).

Firstly, optical losses such as spectrum losses and reflection take the biggest share. The energy of the incident photon is less than the bandgap of the solar cell, it cannot be absorbed. When the bandgap of a solar cell is very smaller than the energy of a photon, the excess energy is removed from the band via thermalization. To reduce losses, the balance between photon energy and bandgap energy must be well adjusted. To overcome this limitation, a semiconductor with a low bandgap and a semiconductor with a high bandgap are combined. Thus, this structure (perovskite/silicon tandem) benefits wide spectra simultaneously. As a result, the efficiency of solar cells can potentially increase.

Energy can be lost due to the recombination of excited carriers via spontaneous emission, that is, electrons and holes can merge and they can emit photons. In this case, the efficiency of the cell is reduced. This is an inevitable process.

Any material above zero Kelvin emits electromagnetic radiation due to blackbody radiation as the temperature rises and this causes energy loss. When solar cells are operated at high temperatures, this loss will more increases.

The maximum voltage and maximum current cannot be achieved simultaneously. It was mentioned before that V_m and I_m are determined by fill factor at a point between I_{SC} and V_{OC}.
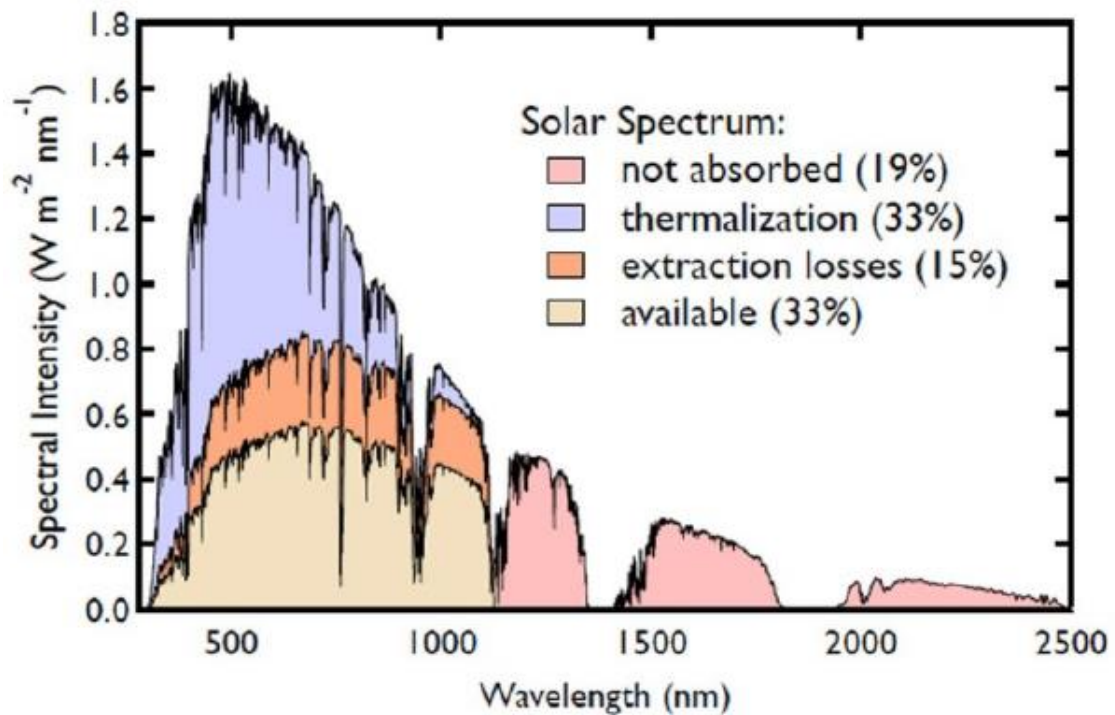
Figure 2. 13 Solar spectrum with energy losses of a silicon solar cell

(Source: Day, Senthilarasu, and Mallick 2019).

2.2 Structure of Perovskite

Essentially, a mineral type that has a different crystal structure was discovered in the Ural Mountains by Gustav Rose in 1839. This mineral was $CaTiO_3$ and was named "Perovskite" due to Lev Perovski who is a Russian mineralogist (Rose 1840). The name of perovskite is used for the structure instead of the mineral. As used today, perovskite is the crystal structure which is represented with ABX_3 formula as shown in Figure 2. 14. The crystal structure of perovskite was identified by Victor Goldschmidt for the first time (Goldschmidt 1926).
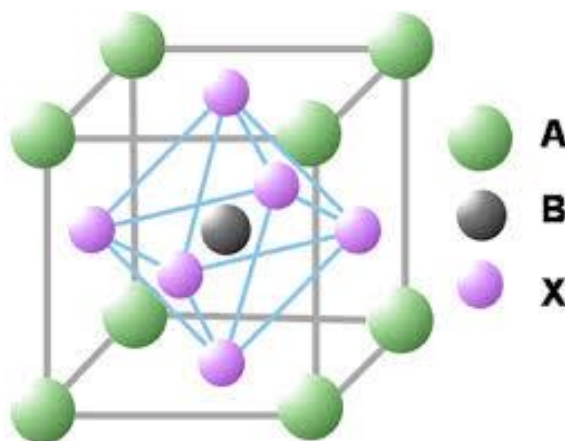
Figure 2. 14 Perovskite crystal structure

In the structure, A and B represent cations, X represents an anion. Perovskite structures with different properties can be created with various elements. With this feature, each perovskite structure can show different electrical, optical, and physical properties. This flexibility has sparked curiosity in scientists, and that is one of the reasons why perovskite is a hot topic.

2.3. Perovskite Solar Cell

Perovskite was used for the first time in solar cell construction in 2009 by Kojima et al. Using the chemical structures $CH_3NH_3PbI_3$ and $CH_3NH_3PbBr_3$, they obtained 3.81% and 3.13% yield, respectively. The layers of the first Perovskite Solar Cell (PSC) were as follows $CH_3NH_3PbI_3/TiO_2$ (mesoporous)/FTO. The stability of this PSC was very weak (Kojima et al. 2009).

In 2012, the efficiency of PSC was increased by adding the hole transport layer to the solar cell structure in two studies (Kim et al. 2012a; M. M. Lee et al. 2012). The PCE of PSCs was 10.9% in Kim's study and was 9.7% in Lee's study. The addition of the new layer caused the creation of long-life carriers in the hole transport layer and reduced the fundamental losses.

Today, the efficiency of PSCs has increased to 25.2% (NREL 2019). This breakthrough, which occurs in a short time like 10 years, is remarkable. Although

Perovskite remains behind its competitors in terms of efficiency and stability, for now, its low-cost production and openness to development give hope for the future.
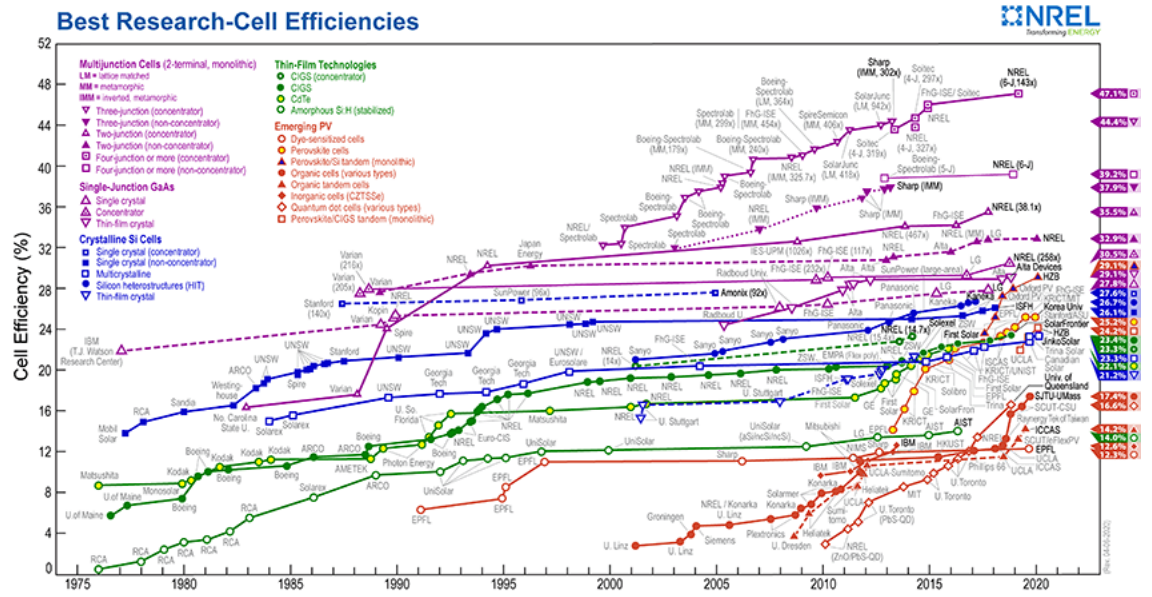
Figure 2. 15 NREL best research-cell efficiencies
(Source: NREL 2019).

2.3.1 Chemical Structure

In the previous section, it was mentioned that the perovskites have ABX_3 structure and what these letters represent. What chemicals perovskite can consist of is summarized in the table below.

Table 2. 1 The common chemical components of perovskite.

A (Organo)	B (Metal)	X (Halide)
Methylammonium (MA)	Pb	Cl
Formamidinium (FA)	Sn	Br
Inorganics		I

Perovskites created using combinations of these components show very different features in terms of bandgap, absorption spectra, stability. Apart from the combinations shown here, different compounds can be created.

The organic compounds that are used in "A" section have some advantages and disadvantages among themselves. The PSCs based on $MAPbI_3$ are not long-term stable under room conditions while their photovoltaic performance is remarkable. When the $MAPbI_3$ layer was exposed to light and oxygen, it is totally degraded at the end of 48 hours. Besides, it is also thermally unstable (Fu et al. 2018; Bryant et al. 2016). The PSCs based on $FAPbI_3$ are stable at high temperatures. Moreover, they have good photovoltaic performance according to $MAPbI_3$ because of their small bandgap that changes between 1.48 and 2.23 eV. Thus, they can absorb wide spectra. The bandgap of $MAPbI_3$ is more than 1.55 eV (Eperon et al. 2014). $FAPbI_3$ passes from the black perovskite phase (α-phase), which has a trigonal symmetry, that occurs after annealing to the unwanted yellow perovskite phase (δ-phase), which has a hexagonal symmetry. The delta phase is undesirable because it reduces the photovoltaic properties of the film (Zheng et al. 2016; Fu et al. 2019). Researchers wanted to eliminate the individual disadvantages by combining methylammonium and formamidinium in different proportions. Pellet et al. escaped the unwanted δ phase by mixing 20% MA in $FAPbI_3$. Furthermore, they achieved 14.9% PCE by mixing 60% $MAPbI_3$ and 40% $FAPbI_3$ (Pellet et al. 2014). Based on this study, Yang et al. reached 19.2% efficiency by mixing 85% FAPbI3 and 15% MAPbI3 (Yang et al. 2015).

In section "B", group IV elements, especially lead, are generally used as metal. The PSCs based on lead, are good at strong absorption in visible regime and have good efficiency, low-cost production and stability, but lead is the toxic and it is harmful for environment (Zhang et al. 2018). Some researchers have sought to substitute a different element for lead. Tin was also used in PSCs and 17% efficiency was obtained with formula $CH_3NH_3SnI_3$, but stability was not as good as the lead based PSCs (Noel et al. 2014). There are also many different studies on lead-free PSCs. In one study, air-stability was improved using the Cs_2SnI_6 formulation, but the efficiency was around 1% (Qiu et al. 2017). In another study, 0.20% PCE was obtained by replacing Pb or Sn with germanium with $MAGeI_3$ absorber layer (Krishnamoorthy et al. 2015).

In the "X" section, halide anions are included. Individually, iodide-based PSCs absorb wider spectra, while bromide and chloride-based PSCs absorb narrower spectra in visible region (Figure 2. 16). It can be understood that the bandgap energy of iodide-based PSCs is smaller than that of others. Bromide-based devices are more stable than iodide-based devices, while they are more efficient than chloride-based devices. On the other

hand, chloride-based devices are more stable than that of others while they are exposed light at room temperature (Figure 2. 17) (Mirershadi, Sattari, and Saridaragh 2018). Since halogens have advantages over each other, the mixed two of these halogens in various proportions enable the band gap energy to be adjusted as desired and created more stable and more efficient PSCs. One of the important studies on this belongs to Jong et al. As a result of the experiments, they acquired efficient and stable device with $MAPb(I_{(1-x)}Br_x)_3$ perovskite by changing x between 0 and 1 and reported the optimal value for x was 0.2 (Jong et al. 2016). In addition, since Astatine (At) is a radioactive and unstable element, it is not used in PSC studies (Fang and Jena 2016).
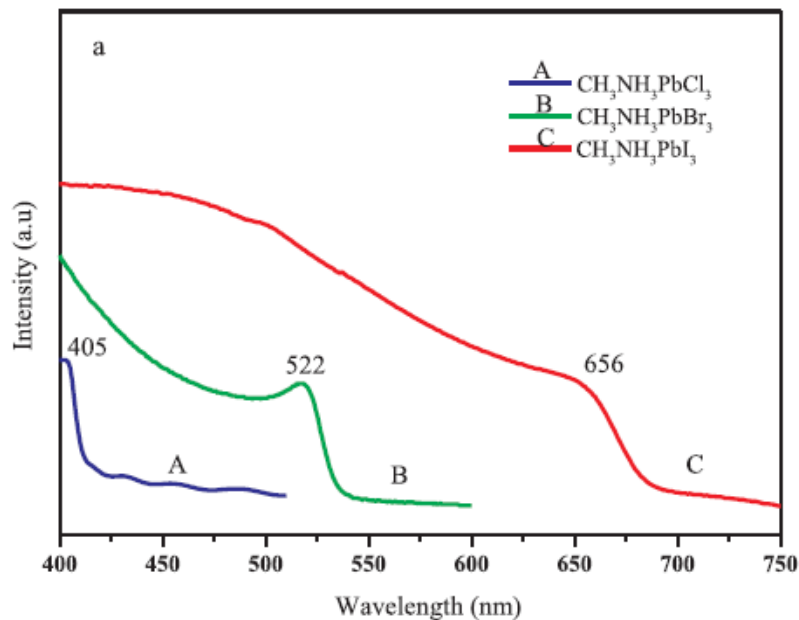
Figure 2. 16 The absorption spectra of $CH_3NH_3PbX_3$ (X = I, Br, and Cl) in visible region (Source: Mirershadi, Sattari, and Saridaragh 2018).
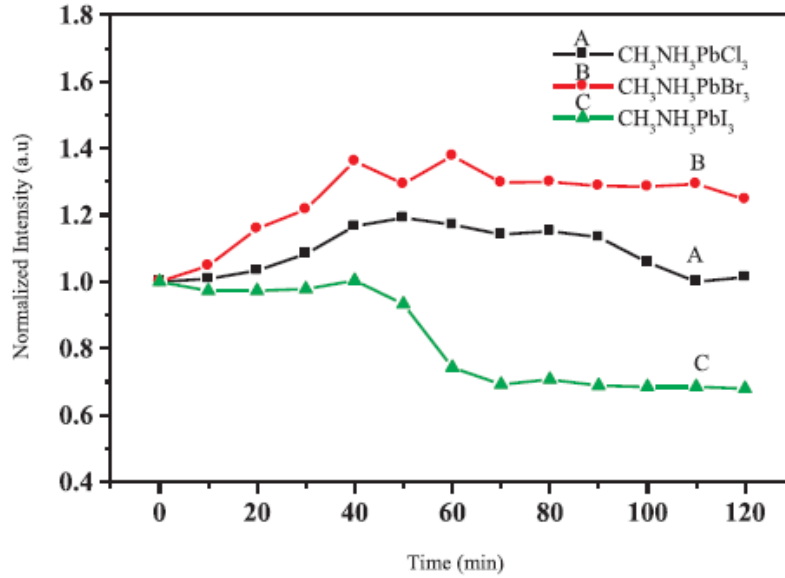
Figure 2. 17 The stability of $CH_3NH_3PbX_3$ (X = I, Br, and Cl) (Source: Mirershadi, Sattari, and Saridaragh 2018).

Besides all this, cesium is added to the mixed-halide perovskite composition as a triple-cation to increase stability and efficiency. Although the devices were exposed to 250 hours of illumination, there was no big decrease in their performance and the PCEs of the devices were more than 20% and thermally stable at the room temperature under the nitrogen atmosphere (Saliba, Matsui, Seo, et al. 2016). The same research group formed the RbCsMAFA perovskite by adding rubidium as the fourth cation in the same year. The devices was able to maintain 95% of their initial performance under 500 °C for 500 hours (Saliba, Matsui, Domanski, et al. 2016).

2D (or layered) perovskites have been used to increase the stability against moisture. They contain large cations and occupy the "A" part in the structure. These cations divide the perovskite structure and form an organic spacer that acts as a 2D quantum well. The bandgap, which is varied depending on the width of organic spacer, of the material can be adjusted by changing the amount of cations. Although 2D perovskites were subjected to 40% moisture for 2 months, no degradation was observed. The PCEs of layered perovskites increased from 4.7% to 18.2% (Cao et al. 2015; Ortiz-Cervantes, Carmona-Monroy, and Solis-Ibarra 2019).
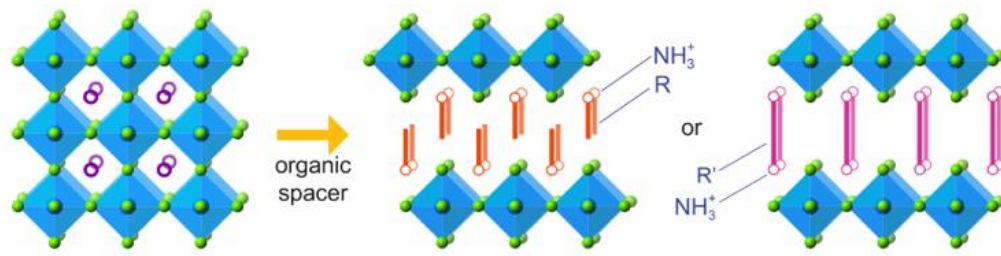
Figure 2. 18 The representation of the formation of layered perovskites (Source: Ortiz-Cervantes, Carmona-Monroy, and Solis-Ibarra 2019).

2.3.2 Fabrication of Perovskite Solar Cells

The modern PSC structure consists of several layers. At the bottom, there is fluorine tin oxide (FTO) or indium tin oxide (ITO) on the glass substrate. For a device in the planar n-i-p architecture, electron transport layer (ETL), which is the n-type layer, is deposited on this structure. These two layers form the anode. The next layer is perovskite, which absorbs light and generates electrons and holes formation. Afterwards, hole transport layer (HTL), which is the p-type layer, is deposited on it. The last layer is the metal which is evaporated onto the structure. HTL and metal contact compose the cathode. Briefly, this modern structure allows the electrons formed in the perovskite layer to pass through the anode via ETL, and the generated holes into the cathode via HTL. In this way, the sunlight turns into electricity. The layers mentioned here need to be explained in detail under this title.

It is possible to replace the layers of PSCs or add the new layers to the PSCs to gain different properties or high efficiency. Adding a mesoporous layer between the ETL and the perovskite layer allows for faster transfer of charges to the anode. The mesoporous layer which acts as a scaffold between layer provides to the device long- term stability thanks to its chemical stability according to regular structure (Meyer 2010; Fakharuddin et al. 2015). In the inverted structure PSCs (p-i-n) is produced by replacing ETL and HTL. Although the efficiency and stability of the inverted structure are not as good as those of traditional PSCs, it has become available on flexible surfaces due to its ability to be formed at low temperatures (T. Liu et al. 2016).
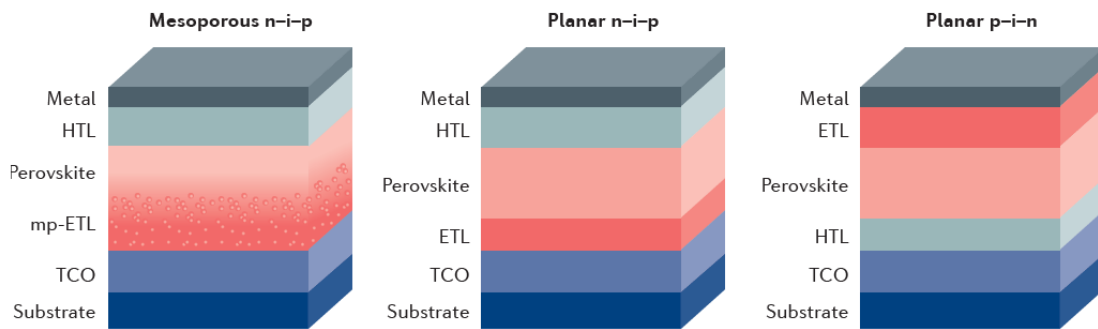
Figure 2. 19 The various structures of perovskite solar cells

(Source: Z. Li et al. 2018).

Several elements can be used for the top metal contact, the top layer of the structure, such as copper, chrome, gold, platinum, silver. In a study on this subject, the efficiency of a PSC in which gold is used as a metal contact is 16.4%, while the efficiency of the closest competitor, platinum-based PSC, is 14.3%. The yield of other metals was very low or they were not chemically unstable. For example, in the experiment where silver was used as a metal contact, the efficiency with the spiro-OMeTAD was 16.5%, but in the HTL-free experiment, the efficiency was 0.17%. The efficiency is naturally related to the suitability with the used HTL layer. Spiro-OMeTAD and gold have a good harmony, usually these two are used together. The reason of this harmony is the transfer of holes to the metal contact efficiently since the working function of gold is 5.1 eV (Behrouznejad et al. 2016).

PEDOT:PSS (poly(3,4-ethylenedioxythiophene) polystyrene sulfonate), spiro-OMeTAD (2,2',7,7'-Tetrakis[N,N-di(4-methoxyphenyl)amino]-9,9'-spirobifluorene), PTAA (Poly[bis(4-phenyl)(2,4,6-trimethylphenyl)amine), PCBM ([6,6]-Phenyl-C61-butyric acid methyl ester) are the most frequently used as the hole transport layer (HTL) materials in perovskite solar cells. The choice of material depends on the structure of the device. While PEDOT is preferred in inverted PSCs (p-i-n) due to its high conductivity and transparency, spiro-OMeTAD, an effective HTL, is used in n-i-p structure (Chen et al. 2015; Fantacci et al. 2011).

In perovskite solar cells, TiO_2, SnO_2, and ZnO, which are enablers carrying electrons to the electrode, are generally used as ETL. The presence of the electron transport layer is significant for the stability of device, blocking holes, and high efficiency. TiO_2 requires high temperatures (about 500°C) for crystallization and has a

good conductivity after crystallization. Therefore, it should be used with FTO (fluorine tin oxide). Compact TiO_2 (c-TiO_2) is used in both planar and mesoporous structures. If there is not well enough coverage, pin holes are formed on the surface due to the roughness of the FTO (about 30nm). The thickness of c-TiO_2 layer should be 65 nm for high performance. ZnO does not require any annealing process for crystallization. With this feature, it can be used on flexible or rigid surfaces. On the other hand, it is not chemical stable, that is, ZnO reacts other weak chemicals. SnO_2 as ETL in PSCs, prevents the degradation of perovskite layer from ambient conditions as it is a stable material. It is annealed at 150°C, which is lower than the temperature required to anneal TiO_2. In addition, Al_2O_3, ZrO_2, m-TiO_2 are used for mesoporous architecture. Al_2O_3 and ZrO_2 are non-ETL which cannot too much electron, but they increase V_{OC} due to energy band lineage. However, they have poor stability and suffer from hysteresis effect (Mohamad Noh et al. 2018).

Lastly, indium tin oxide (ITO) degrades at high temperatures and losses its conductivity. FTO is resistant to high temperatures (until 700°C), but its surface is rougher than that of ITO.

2.3.3 The Control of Crystallization

When perovskite solution is left on the substrate, thermal energy increases due to the given heat, and the perovskite film starts to nucleate. As the temperature increases, nucleation also increases. Then, these nuclei grow and form crystals, and this process continues until the material runs out. The sizes of these crystals have an important place for the efficiency of the device. In an efficient device, these crystal grain sizes range from 400 to 1500 nanometers and these crystal grains should be uniformly distributed over the substrate. Since grain boundaries decrease the performance of the device, large grains are desired (Y. Zhou et al. 2015; B. Liu et al. 2019). There are several methods for growing crystals. Although size control of the crystal is generally provided by temperature, the antisolvent quenching method is an important method for crystallization. This technique will be detailed in Chapter 2.5.
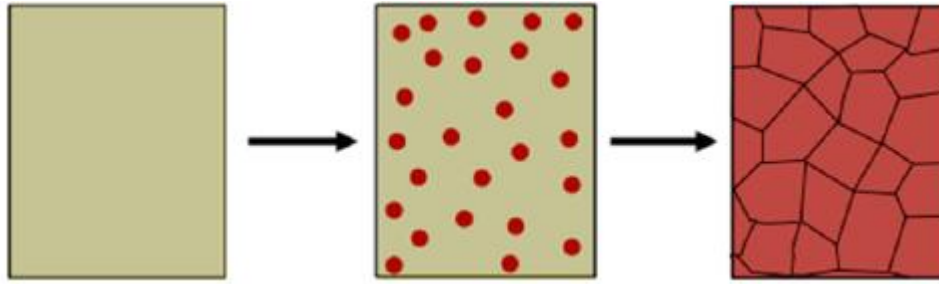
Figure 2. 20 The illustration of the nucleation and the growth of grains uniformly
(Source: Y. Zhou et al. 2016).

While heating the precursor solution and annealing after the coating are the significant technique for spin coating deposition, heating the substrate and sintering after the deposition are the preferred methods for spray cast deposition. Zhou et al. heated the precursor solution at different temperatures before spin coating, and then anneal at 90°C and observed its effect on crystal sizes. They found out that the largest grain sizes occurred at temperatures of 80-85°C as in Figure 2.21 (X. Zhou et al. 2018).
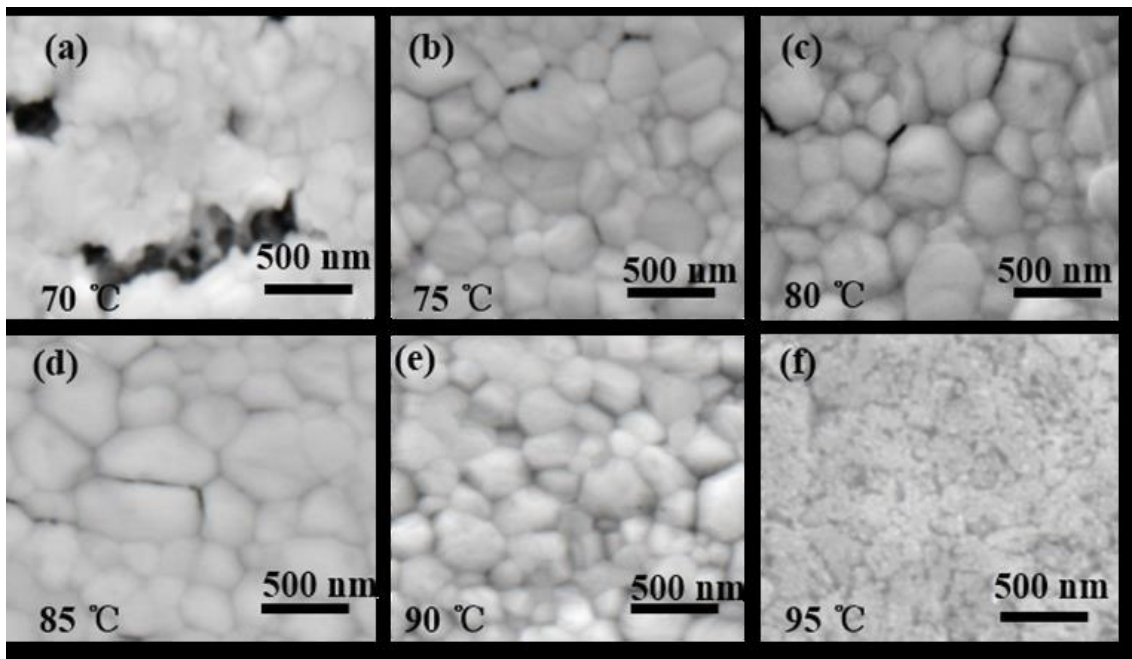
Figure 2. 21 The various grain size of the perovskite films according to the temperature of the precursor solution (Source: X. Zhou et al. 2018).

Post-deposition sintering is a common process in both deposition techniques for removing solvents from the film and forming uniformity. A research group conducted a study on film morphology and efficiency of annealing temperature. They reported that the minimum temperature should be 80°C to create the $CH_3NH_3PbI_3$ perovskite. At temperatures below this minimum value, the solvent was removed from the film, but they could not observe the formation of perovskite. They indicated that the optimum temperature for perovskite formation and uniform morphology should be between 80-100°C and reported that the film returned to δ-phase again at temperatures above 150°C. (Dualeh, Tétreault, et al. 2014).

2.3.4 Stability

Stability is the strongest obstacle in the commercialization of PSCs. Research focuses on creating a thermally stable, long term stable, and phase stable device. These instabilities are tried to be eliminated by changing ABX_3 components, encapsulation, nitrogenous environment, adjusting environmental conditions, and proper selection of layers. The phase stability of the perovskite layer, which is one of the stabilities that is crucial to adjust, can be calculated with the Goldschmidt tolerance factor as follows:

$$t = \frac{R_A + R_X}{\sqrt{2}(R_B + R_X)} \tag{2.11}$$

Here, t is the tolerance factor, R_A, R_B, and R_X are the ionic radii of A, B, and X ions. The t value of a stable perovskite structure at room temperature is between 0.81 and 1.11. For an ideal cubic perovskite structure, this value is between 0.90 and 1.0. The desired t value, which is required for more stable and cubic perovskite structure, can be obtained by including ions of different sizes in the structure (D. Wang et al. 2016).

2.3.5 Current-Voltage Hysteresis

I-V hysteresis is still an unsolved issue that affects the stability and efficiency of PSCs. Hysteresis is the mismatch between the curve of forward scan (from 0V to V_{OC}) and that of the reverse scan (from V_{OC} to 0V) as shown in Figure 2.22.
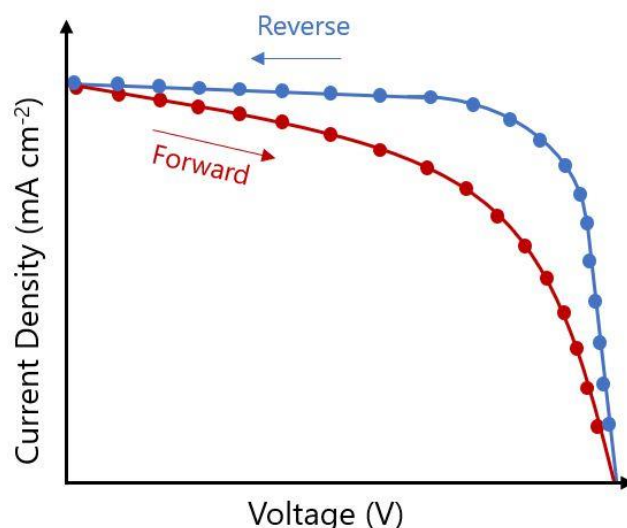
Figure 2. 22 The example of I-V hysteresis.

This negative factor in PSCs was first reported in 2014 (Dualeh, Moehl, et al. 2014). Another research group, which is investigating origination of this problem, based on the formation of hysteresis on three parameters. The first was that the defects on the perovskite layer act as a trap for charges at high scanning speeds. Scanning should be done slowly to prevent this situation. The second was slow polarization depending on biased voltage because of the ferroelectric properties of perovskites. The last one was the migration of the excess ions and this can be adjusted by material selection. (Snaith et al. 2014). Later research has shown that ion movements affect hysteresis rather than ferroelectricity (Meloni et al. 2016).

2.3.6 Deposition Techniques

Today perovskite solar cells are created by various techniques. In this section, the most frequently used of these techniques will be explained. The spray cast deposition used in this thesis will be detailed in a separate section.

Spin coating is based on dropping the solution onto the substrate. The spin coater then starts spinning the substrate at a few thousand revolutions per minute (rpm). In this way, the solution is spread uniformly throughout the substrate and the spinning provides

to remove some of the solvents such as DMF (dimethylformamide). The rotational speed and the thickness of the formed film are inversely proportional. Then the perovskite film is put on the hot plate between 100-120°C for 10-20 minutes to anneal. This process is necessary for the removal of the remaining solvent and crystallization. The morphology of the films produced with this method is very smooth. The highest efficient devices have been produced with this technique up to the present.

Depositing the   **Rotational**   **Evaporation of**
solution   **spreading out**   **solvent**
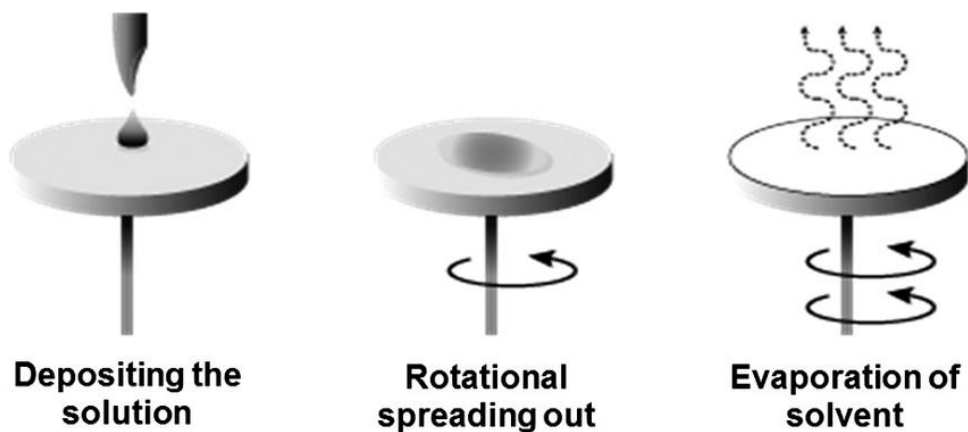
Figure 2. 23 The spin coating process (Source: Amokrane et al. 2018).

On the other hand, a lot of material is wasted during the casting process. Therefore, the spin coating is not a scalable, economically viable and green technique. Moreover, it is not appropriate to use this method for large-area devices. These disadvantages prevent the commercialization of this technique.

The yields of PSCs produced by scalable methods are lower than those produced by spin-coating. However, with the recent studies, the difference has started to close. Production costs must be low for PSCs to be commercialized. Material waste should be minimized to reduce production costs. This can be accomplished with scalable methods. Some important scalable methods are; slot-die coating, spray-coating, blade-coating, inkjet printing.

Slot-die coating, a scalable technique, relies on a head moving across the substrate to release the strip-shaped solution. Another head from the back of the solution head gives high-pressure nitrogen to dry the solution. A heated substrate or ultrasonic substrate vibration can be used for the same purpose. With this method, all layers of a PSC can be created uniformly. Since high temperatures are required for the mesoporous scaffold, it can only be used for a planar structure. This technique is suitable for use on flexible

surfaces. Growing crystals is a big problem for this method since it is difficult to dry the film. Despite this difficulty, 18% efficiency has been achieved (Hwang et al. 2015; Whitaker et al. 2018).
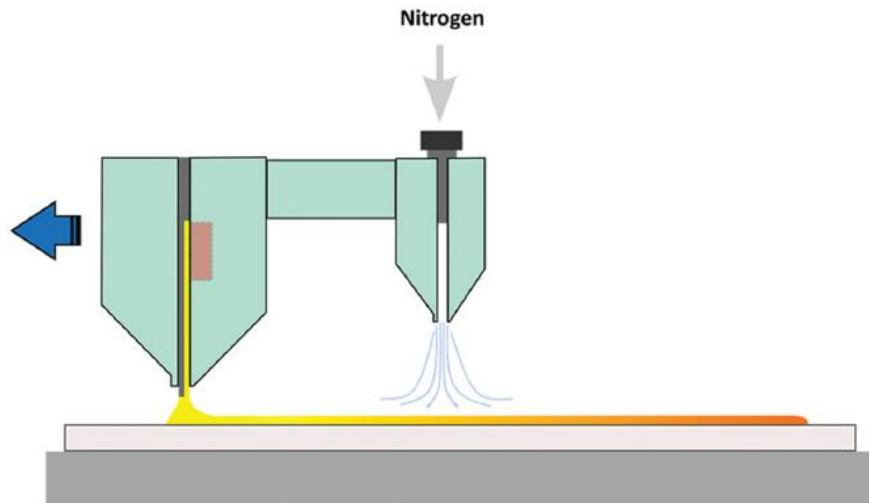
Figure 2. 24 The schematic illustration of the slot-die coating
(Source: Hwang et al. 2015).

Blade coating or doctor blading, which can be used for large-area coating, is the low-cost scalable deposition method that relies on sliding a blade that stands at a certain height to finely coat a solution on the substrate. The solvent is then evaporated to begin crystallization. These methods have achieved 20.2% efficiency in small-area PSCs (Wu et al. 2018).
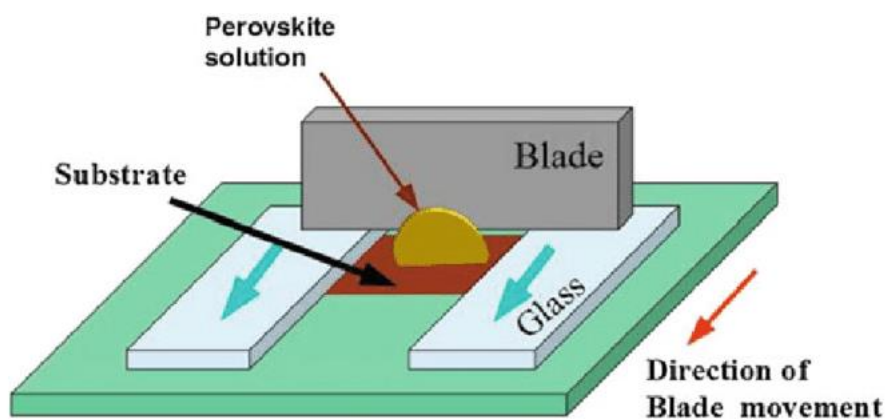
Figure 2. 25 The schematic illustration of blade coating
(Source: Kajal, Ghosh, and Powar 2018).

The ink put on the screen is transferred to the substrate in a certain pattern through the pores of a screen (mesh) via a squeegee. The quantity of the solution deposited on the substrate can be adjusted by changing the thickness of the screen. However, the thickness control is not easy for thin films. This scalable method is called screen printing (serigraphy) and can be used in large-area (Rong et al. 2018).
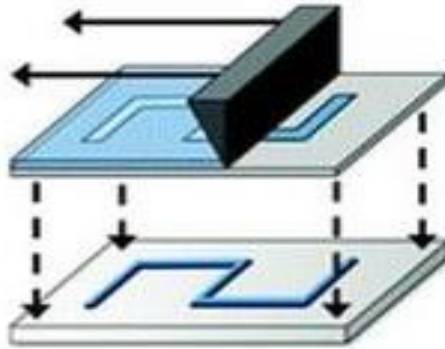
Figure 2. 26 The schematic illustration of screen printing
(Source: Saliba et al. 2018).

Inkjet printing is a scalable, high controlled deposition method that can be applied in flexible and large areas. Perovskite solution is delivered to a nozzle continuously. The solution comes to the piezoelectric transductor in the nozzle and is divided into droplets. The droplets are uniformly distributed on the substrate in certain patterns via the nozzle and the moving substrate. Perovskite solution passes to the α-phase under post-treatment. Eggers et al. deposited the triple-cation perovskite solution with the inkjet method in a thickness of more than 1 μm and reached above 21% PCE (Eggers et al. 2020).
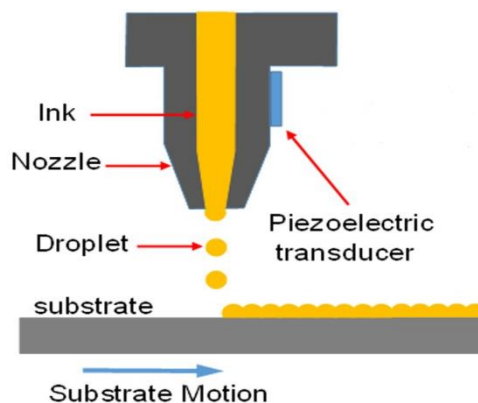
Figure 2. 27 The schematic illustration of inkjet printing (Source: "Inkjet Printing Process for Kesterite Solar Cells" n.d.).

In 2013, dual-source vapor deposition was used to deposit the $CH_3NH_3PbI_{(3-x)}Cl_x$ perovskite in nitrogen ambient. MAI (organic salt) and PbCl2 (inorganic salt) were evaporated simultaneously above the FTO/TiO2 structure on the pot rotating above at molar ratio of 4: 1 from separate sources. Then, spiro-OMeTAD was coated on it by spin-coating. 15.4% peak efficiency was obtained from the device created with this technique (M. Liu, Johnston, and Snaith 2013).
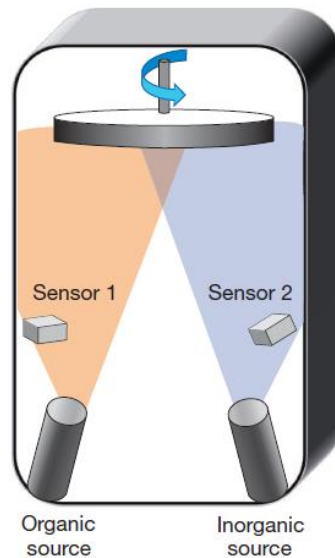
Figure 2. 28 The schematic illustration of dual-source vapor deposition
(Source: M. Liu, Johnston, and Snaith 2013).

As a result, spin coating is a method that can only be used in small areas and cannot be scaled, but the most efficient devices are produced with this method. On the other hand, scalable methods exceed 20% efficiencies, and their stability increases with various arrangements such as the control of the relative humidity and ambient temperature. The highest efficiencies can be achieved with devices smaller than 1 cm^2. As of today, high efficiency and strong stability cannot be achieved in large-area devices. This development shows that PSCs produced by scalable methods may be commercialized in the coming years.

Table 2. 2 Summary of the data of highly efficient PSCs made with scalable methods.

Active Area (cm^2)	V$_{OC}$ (V)	Jsc (mA/cm^2)	FF	PCE	Device Structure	Processing Method	Reference
0.105	1.11	24.6	80	21.6	ITO/NiOx/Cs$_{0.1}$MA$_{0.15}$FA$_{0.75}$Pb(I$_{0.85}$Br$_{0.15}$)$_3$/C$_{60}$/ Bathocuproine (BCP)/Au	Inkjet Printing	(Eggers et al. 2020)
1	-	-	-	10.4	ITO/NiOx/Cs$_{0.1}$MA$_{0.15}$FA$_{0.75}$Pb(I$_{0.85}$Br$_{0.15}$)$_3$/C$_{60}$/ Bathocuproine (BCP)/Au	Inkjet Printing	(Eggers et al. 2020)
0.08	1.1	22.7	81	20.2	ITO/MAPbI$_3$:F4TCNQ(2,3,5,6-Tetrafluoro-tetracyanoquinodimethane)/C$_{60}$/BCP/Cu	Blade Coating	(Wu et al. 2018)
0.06	1.1	21.5	76	18	ITO/SnO$_2$/MAPbI$_3$/Spiro-OMeTAD/Au	Slot-die Coating	(Whitaker et al. 2018)
0.025	1.09	23.1	77	19.4	ITO/np-SnO$_2$/ Cs$_{0.05}$FA$_{0.81}$MA$_{0.14}$Pb(I$_{0.85}$Br$_{0.15}$)$_3$ /Spiro-OMeTAD/Au	Spray Coating	(Bishop et al. 2020)
0.154	1.12	23.8	61	16.3	ITO/np-SnO$_2$/ Cs$_{0.05}$FA$_{0.81}$MA$_{0.14}$Pb(I$_{0.85}$Br$_{0.15}$)$_3$ /Spiro-OMeTAD/Au	Spray Coating	(Bishop et al. 2020)
1.08	-	-	-	12.7	ITO/np-SnO$_2$/ Cs$_{0.05}$FA$_{0.81}$MA$_{0.14}$Pb(I$_{0.85}$Br$_{0.15}$)$_3$ /Spiro-OMeTAD/Au	Spray Coating	(Bishop et al. 2020)

2.4. Spray-Cast Perovskite Solar Cell

Spray deposition, which is scalable and used for large areas, is a deposition technique that based on casting droplets onto a hot substrate with the aid of carrier gas. These droplets are formed by a nozzle that vibrates at high frequencies and separates the incoming solution into small pieces. To ensure homogeneity, droplets resembling mist must completely cover the hot substrate. The dried film is then annealed at a higher temperature for crystallization.
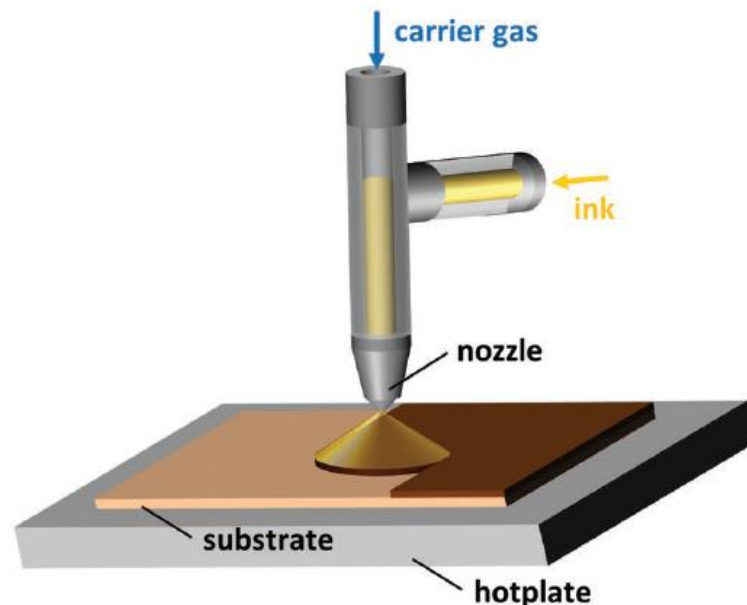
Figure 2. 29 The schematic illustration of spray-cast deposition
(Source: Howard et al. 2019).

One of the first spray-cast perovskite solar cell study was performed by Barrows et al, using the $CH_3NH_3PbI_{(3-x)}Cl_x$ perovskite solution under ambient conditions. They used the ITO/PEDOT:PSS/Perovskite/PCBM/Ca/Al inverted structure and achieved above 11% PCE (Barrows et al. 2014).

Mohamad et al. reached 9.9% efficiency with an inverted architecture by covering HTL, ETL, and absorber layer ($CH_3NH_3PbI_{(3-x)}Cl_x$) with spray-coating under ambient condition. Using the same materials, they covered these layers with spin-coating under a nitrogen atmosphere. Here they achieved 12.8% efficiency. They attributed the loss of yield to spray reduction to homogeneity and lower surface coverage (Mohamad et al. 2016).

Bishop et al. deposited a normal architectural device (FTO/c-TiO$_2$/m-TiO$_2$/ $CH_3NH_3PbI_{(3-x)}Cl_x$/Spiro-OMeTAD/Au) under environmental conditions and achieved 10.2% PCE peak for spray-coated ETL,HTL, and the perovskite layer. Then, they produced large area devices ($\geq 1cm^2$) with the same process and obtained 6.6% PCE (Bishop et al. 2017).

A two-step spray method was used by Huang et al. to increase efficiency and acquire smoothness. For the first step, PbI$_2$ dissolved in DMSO (dimethyl sulfoxide) was cast onto the FTO/TiO$_2$ substrate and dried at 60°C. When the film at 80°C, the MAI solution was then sprayed onto the film and the temperature was raised to 115°C to increase diffusion. The film was then washed with isopropanol and the MAI on the surface was removed and the film was subjected to 100°C for 2 hours. As a result of this process, the conversion from PbI$_2$ to MAIPbI$_3$ was completed. The PCE obtained in this study was 16.3% for small areas and 13.9% for large areas (1 cm^2) (Huang et al. 2016).
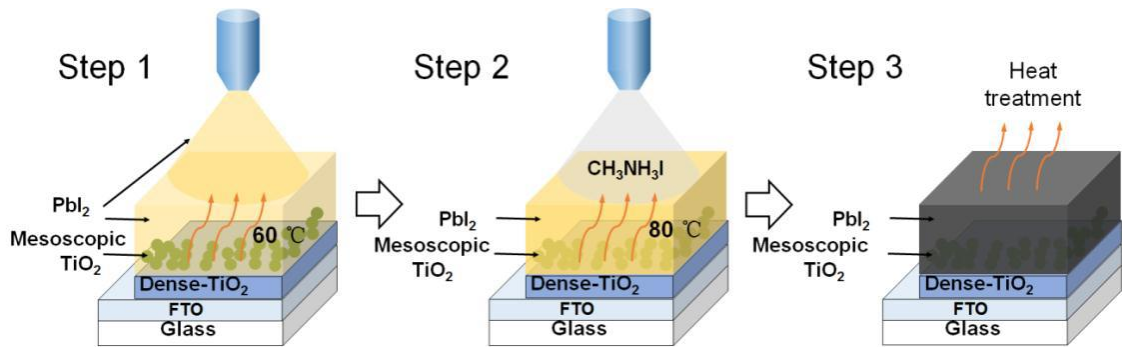
Figure 2. 30 The schematic illustration of two-step spray-casting

(Source: Huang et al. 2016).

By controlled the crystal grain growth, %18.3 peak PCE is obtained with normal structure (FTO/TiO2/MAPbI$_{(3-x)}$Cl$_{(x)}$/PTAA/Au) in 2016. This yield was a record and they held this record for 4 years (Heo et al. 2016).

As of April 2020, the highest achieved PCE for spray-casting devices is 19.4%. This record was broken in fully spray-coated normal structure (ITO/np-SnO$_2$/perovskite/spiro-OMeTAD/Au) using triple-cation perovskite (Cs$_{0.05}$FA$_{0.81}$MA$_{0.14}$PbI$_{2.55}$Br$_{0.45}$) for small-area device (2.5 mm^2). They used the vacuum flash assisted solution processing (VASP) method after deposition of the absorber layer to control crystallization. This method removes the DMF from the film, resulting in a partially crystallized layer. In addition, they achieved 12.7% PCE at 1.08 cm^2 area by connecting 7 devices (each with an area of 15.4 mm^2) in parallel on a substrate (Bishop et al. 2018; 2020).

By changing some parameters or appending novelties, spray-cast deposition improves day by day. There are some basic considerations such as wetting, crystalline grain growth, annealing to increase the performance of a device with this method.

2.4.1 Wetting

Wetting is an important phenomenon in terms of completely covering the substrate with a solution. Sprayed droplets should fall onto the substrate with the correct contact angle. The contact angle should be small for a good coating.
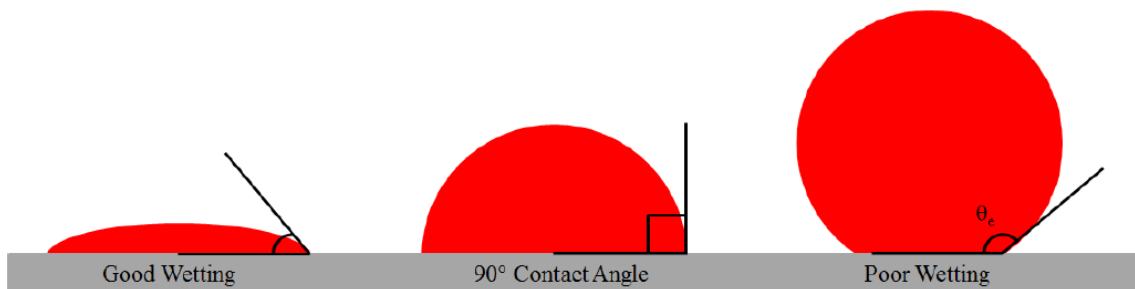
Figure 2. 31 The schematic illustration of the contact angles of three droplets on a solid substrate.

The contact angle (Q_e) can be calculated with the formula below,

$$\cos(Q_e) = \frac{\gamma_{SA} - \gamma_{SL}}{\gamma_{LA}} \tag{2.12}$$

Here, γ_{SA} is the interfacial energy between solid and air, γ_{SL} is the interfacial energy between solid and liquid, and γ_{LA} is the interfacial energy between liquid and air (De Gennes 1985). If the contact angle is greater than 90°, this is called a hydrophobic coating, and if it is less than 90°, this is called a hydrophilic coating.

The contact angle should be equal to 0 for the ideal case (super hydrophilic coating). In this case, the equation becomes:

$$\gamma_{SA} - \gamma_{SL} = \gamma_{LA} \tag{2.13}$$

To approach the ideal case, the solution which has low surface tension, and the substrate which has a high surface tension should be chosen.

2.4.2 Crystalline Grain Growth

Crystalline grain growth, which is one of the factors affecting the performance of the device, can be improved by changing some parameters in spray-coating. These changes are defined with the balance between inward flux (F_{in}) and outward flux (F_{out}) by Heo et al. F_{in} represents the concentration and amount of precursor solution falling on the substrate and F_{out} represents solvents that evaporate from the substrate. As is known, DMF and DMSO are frequently used in perovskite solutions as solvents. DMF is a solvent that evaporates quickly and evaporates during spraying without falling into the hot plate. However, DMSO is a slowly evaporating solvent and it vaporizes from the film when it falls into a hot substrate. In this respect, DMSO has an effect that delays crystallization, and this feature is used to establish the balance between F_{in} and F_{out}.

The solvent evaporation represents outward flux and the continuity of the precursor solution represents inward flux as shown in Figure 2.32 (a). The balance between F_{in} and F_{out}, which can be adjusted with solution concentration, flow rate, solvent mixture, and substrate temperature, determines the crystal grain size (Heo et al. 2016).
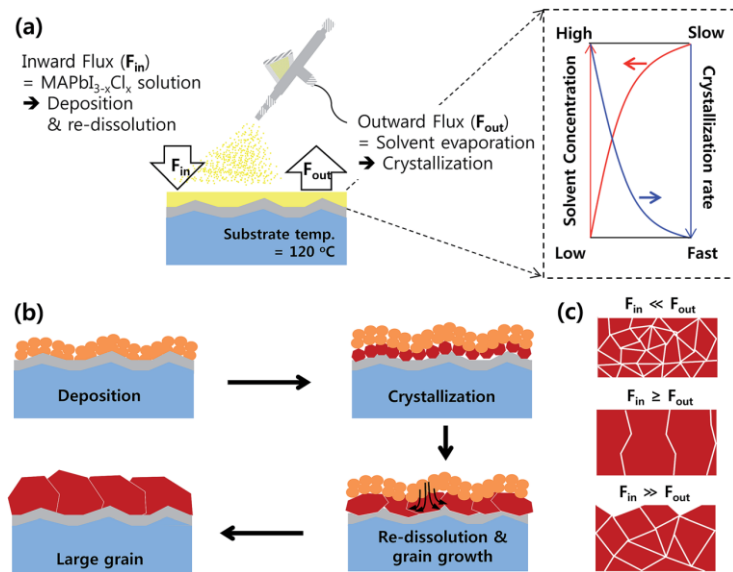
Figure 2. 32 The schematic illustration of (a) the mechanism of spray-coating, (b) the crystallization formation and the grain growth, (c) the morphology that changes depending on the balance between F_{in} and F_{out} (Source: Heo et al. 2016).

In the case of $F_{in} << F_{out}$, as soon as the first droplets contact the surface, they dry and crystallize and form a film. Subsequent droplets also suffer from the same result. Thus, small crystalline grains are obtained and the absorber layer does not perform well.

In the case of $F_{in} >> F_{out}$, when the first droplets fall into the substrate, they merge with subsequent droplets before the crystallization begins. The formed wet perovskite film needs to heat-treatment. After the heating process, a rough surface and small grains are obtained.

In the case of $F_{in} \geq F_{out}$, while the first sprayed droplets begin to crystallize, they combine with the subsequent droplets to form large grains. By providing this equilibrium, high quality absorber layer can be obtained. As mentioned earlier, high performance devices have continuous large grains.

2.4.3 The Substrate Temperature and Annealing Process

The droplets begin to crystallize when they drop onto a hot substrate. The higher the substrate temperature, the smaller the particle size. Barrows et al. sprayed $CH_3NH_3PbI_{(3-x)}Cl_x$ perovskite on the substrate at different temperatures under ambient conditions. Then, they annealed for 90 minutes at 90°C (Barrows et al. 2014). The results are as seen in Figure 2.33. The precursor solution sprayed on the substrate held at 28°C and 30°C formed discontinuous crystalline areas after treatment and did not have good surface coverage. They observed that as the temperature increased, the surface coating improved and continuous crystalline areas were formed. They reported that the surface coverage of the film formed on the substrate at 75°C was the best coverage they achieved.
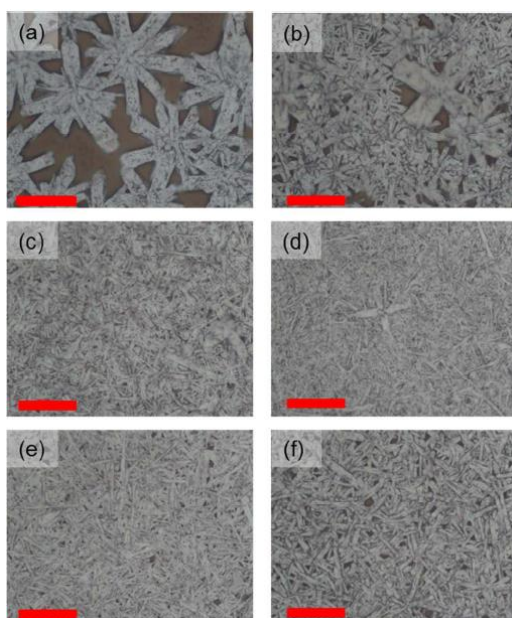
Figure 2. 33 The optical microscope images of the perovskite film on the substrate at different temperatures. (a) 28 °C, (b) 38 °C, (c) 55 °C, (d) 75 °C, (e) 80 °C, (f) 87 °C. The red bar represents 20 μm length (Source: Barrows et al. 2014).

Annealing is the process in which solvents are removed from the film and crystallization is completed. Annealing temperature and duration are the parameters that determine the quality of the film. Dualeh et al. conducted research on the effect of annealing temperature on the $CH_3NH_3PbI_3$ perovskite film created by spin-coating. Annealing duration was long at low temperatures and short at high temperatures. They

obtained the highest absorbance from the film annealed at 100°C for 45 minutes (Dualeh, Tétreault, et al. 2014). On the other hand, it is reported that the $CH_3NH_3PbI_3$ precursor solution needs to be annealed at 100°C for 15 minutes to switch to perovskite form (Kim et al. 2012b). The annealing process does not much change in spray-coating. In general, annealing temperature is between 100°C and 120°C; annealing time is between 10 and 20 minutes for spray-coating.

2.5. Antisolvent Quenching

The most important factor that determines the performance of a perovskite film is high-quality crystallization. Antisolvent quenching, which was first used in 2014 for, is a method commonly used with spin-coating to improve the morphology of the surface and develop crystallization. It makes these developments by removing the solvents, such as gBL, DMF, and DMSO, in the precursor solution. Diethyl ether (DE), chlorobenzene (CBZ), chloroform (CF), xylene (XYL), toluene (TL), trifluorotoluene (TFT), 2-prophanol (IPA), acetonitrile (ACN), dichloromethane (DCM) are some of the antisolvents.

In the first PSC study using this method, toluene was dropped on the $CH_3NH_3PbI_{(3-x)}Br_x$ (x=0.1-0.15) perovskite film while the precursor solution covers the substrate surface during the spinning. The pouring of toluene causes the removal of DMSO and uniform surface morphology. The intermediate phase is then formed (as seen in Figure 2.33). Finally, this film is annealed at 100 °C for 10 minutes and the absorber layer is created completely. They received 16.3% efficiency from the device they created with normal architecture (FTO/c-TiO_2/m-TiO_2/Perovskite/PTAA/Au) and did not observe hysteresis (Jeon et al. 2014).
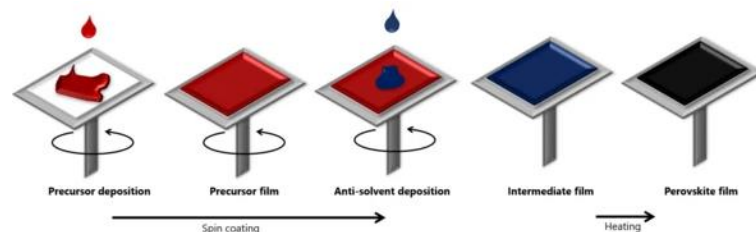
Figure 2. 34 The schematic illustration of the antisolvent quenching (Source: "Perovskites & Perovskite Solar Cell Structure, Efficiency and More | Ossila" n.d.).

An important point in antisolvent quenching is timing. Antisolvent should be dropped onto the film after the solution has finished spreading over the substrate. Dropping after the film dries is also useless. The timing issue has been the subject of a study. The solution is spread on the rotating substrate at 5000 rpm in 3 seconds and the excess precursor solution is removed from the film. Antisolvent cast after the seventh second does not affect the crystallization process (Xiao et al. 2014). When the antisolvent is dropped at the right time, the transparent film turns cloudy. This time point is called a turbid point (F. Wang et al. 2019).

In 2015, Ahn et al. dropped DE on $CH_3NH_3PbI_3$ solution and first heated it at 65°C for 1 minute, then sintered at 100°C for 2 minutes. As a result, they achieved a 19.3% PCE peak. They reported that DE is a more suitable antisolvent because it is immiscible with DMSO, unlike toluene and chlorobenzene (Ahn et al. 2015). Li et al. made a comparison by pouring TL, DE, and DCM onto $CH_3NH_3PbI_3$ perovskite at similar rates and times. The perovskite film with DE is pinhole-free, while large and small pinholes are formed in other films (Y. Li et al. 2017). It is thought that because of DE does not mix with DMSO, creates a homogeneous intermediate phase that delays rapid nucleation (Konstantakou et al. 2017). It should also be noted that these different antisolvents that are poured at the same time are not only dependent on their non-mixing property. Antisolvents have individual poured-time to interact with the precursor solution (Paek et al. 2017).

Antisolvent is not only dropped during spin-coating, but there are also other methods. Jang et al. immersed the $CH_3NH_3PbI_3$ perovskite in the antisolvent bath (DE) at 0°C and then annealed the film. By this method, they reached 17% efficiency (Jang et al. 2019). Lee et al. achieved 20.1% PCE by spraying a 4: 1 mixture of CB and ACN on perovskite film formed via spin-coating. ACN helps to protect the morphology of the film and CBZ eases the nucleation. The resulting pinhole-free films had large grains (D. S. Lee et al. 2020).

CHAPTER 3

THE NOVEL DEPOSITION SYSTEM

Since our system is completely unique, it needs to be introduced in detail. This section will be described in three parts. In the first part, the production of antisolvent vapor is explained. The ultrasonic spray coating will be explained in the second part. In the third part, the operation of the novel antisolvent-assisted ultrasonic spray coating system will be explained. The main purpose of the system is to benefit from the antisolvent method, which is generally used in spin-coating, and adapt it to ultrasonic spray coating with the necessary modifications.

3.1. The Production of Antisolvent Vapor

A hot plate with a stirring feature heats the glycerin, that helps us to control the temperature of our bubbler with liquid antisolvent in it. The temperature of the glycerin should be equal to the boiling point of the antisolvent for adequate vapor production. The reason for using glycerin is that it has a higher boiling point (290°C) than that of antisolvents. If the temperature is high, the antisolvent boils and evaporates quickly. Therefore, the temperature control of the system is critical. Moreover, nitrogen is sent to the inlet of the bubbler as the carrier gas. This helps us mix the antisolvent vapor with nitrogen. The nitrogen and antisolvent vapor mixture are then fed into the ultrasonic spray nozzle through the fan air inlet.
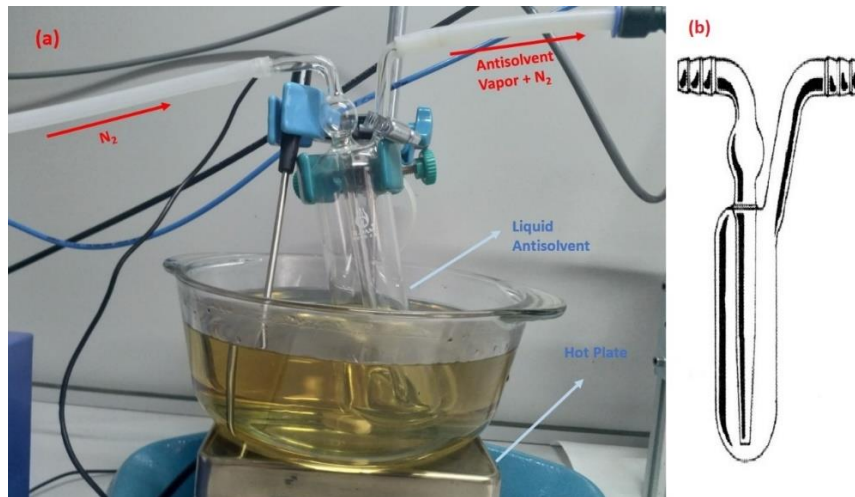
Figure 3. 1 Antisolvent vapor generation system (a) general view of the system, (b) the illustration of a bubbler.

3.2. The System of Spray-Coating

As can be seen in Figure 3. 2, this ultrasonic spray that we use in our experiments has two fan air inlets, an axial air inlet, cooling air in, cooling air out, RP-SMA (Reverse-polarity Sub Miniature version A) connector inlet, and a hole where the solution enters in the middle.
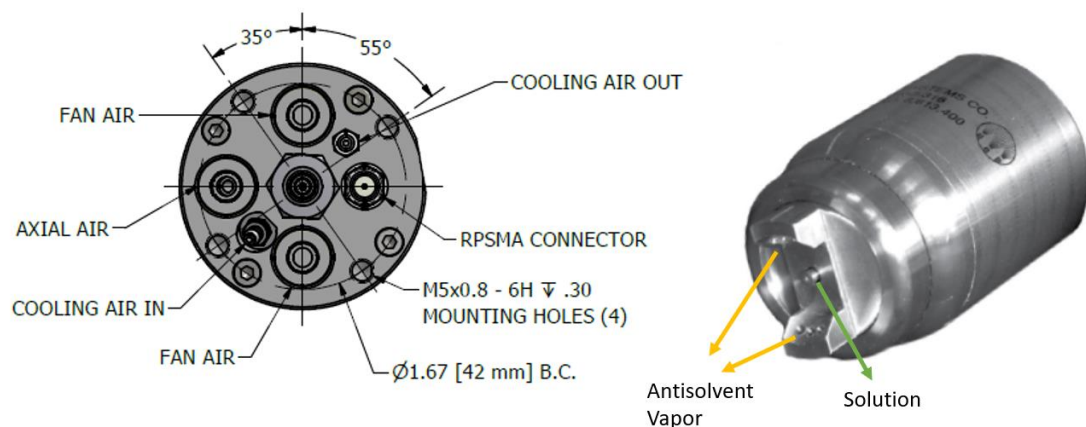
Figure 3. 2 The ultrasonic spray.

The antisolvent vapor and nitrogen mixture enters the system from the fan air inlets. The axial air inlet is connected to a nitrogen cylinder. Enough nitrogen flow through this inlet allow us pushes the solution droplets onto the substrate. The spray

temperature increases because of the electrical to mechanical energy conversion in the ultrasonic nozzle. Therefore, cooling air is necessary to operate the nozzle for long times. The cooling air enters the nozzle from "cooling air in" and is discharged from "cooling air out". RP-SMA is an RF connector that connects the spray nozzle with an ultrasonic generator to provide ultrasonic vibration and ultimately atomization. The solution inlet is provided by tubing connected to a glass syringe that is driven by a syringe pump. The flow rate of the solution is provided by a syringe pump on which the glass syringe is located. The range of flow rate is determined by the orifice diameter of the ultrasonic nozzle. For our nozzle orifice diameter is 0.012 and the flow rate range is 0.04-2 ml/min.

We have a motion system that allows the spray to move in the x-y plane. This motion system is connected to a computer. The speed of the spray nozzle and the pattern of the sprayed solution can be adjusted from the computer.
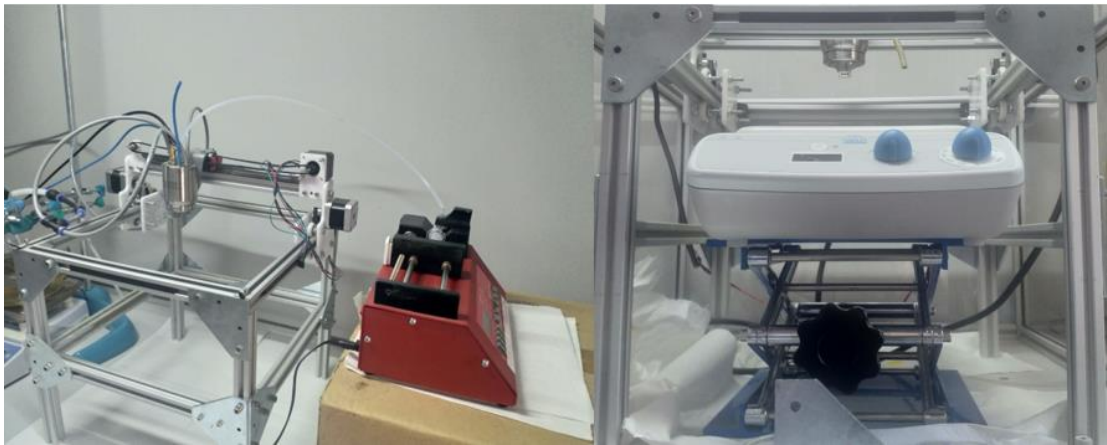
Figure 3. 3 The dynamic spray system, syringe pump, and the lab jack.

We place a hot plate under the spray nozzle to control the substrate temperature. The distance between the spray and the hot plate is controlled by a lab jack. Another hot plate is included in the system for annealing after deposition.

Figure 3. 4 Hot plates used in the experiment, (a) to control the substrate temperature, (b) to anneal our samples.

3.3. The Operation Principles of The Antisolvent-Assisted Ultrasonic Spray System

The temperature of the hot plate under the glycerin filled container is brought to the boiling point of the antisolvent inside the bubbler and the antisolvent starts to evaporate. Nitrogen is supplied from the nitrogen tubes connected to "Axial air" and "Fan air". Spray nozzle and ultrasonic generator connections are made through the RF cable and RP-SMA connector, thereby the nozzle is prepared for vibration at high frequencies (75kHz). At high frequencies, ultrasonic vibration is essential to break the solution into droplets (i.e. ultrasonic atomization). Then, the flow rate is adjusted using the syringe pump. The flow rate should be selected low enough so that the solution does not over-wet the substrate surface. Excessive wetness on the surface causes the morphology of the film to deteriorate. The speed and direction of the spray are adjusted from the computer by controlling the rotation speed of stepper motors. The spray should move at y-axis for antisolvent-solution interaction and at slow speeds so that the precursor solution completely covers the substrate surface. In our experience, to achieve the highest homogeneity, the ultrasonic spray must move, and the deposition must be done in a single spray pass. After all preparations are completed, the ultrasonic generator, syringe pump, and motion system are operated simultaneously, allowing the droplets to fall on the substrate that is kept at elevated temperature (typically at 75 ℃). Droplets that fall on the

substrate regularly, form a film and this film will wait for a while to dry. The dried film is put on another hot plate at a higher temperature (typically at 100°C) for annealing and complete crystallization. As a result of annealing, crystallization is achieved, and perovskite is formed.

Since perovskite-antisolvent interaction is the subject in this thesis, only the perovskite layer is spray-coated.
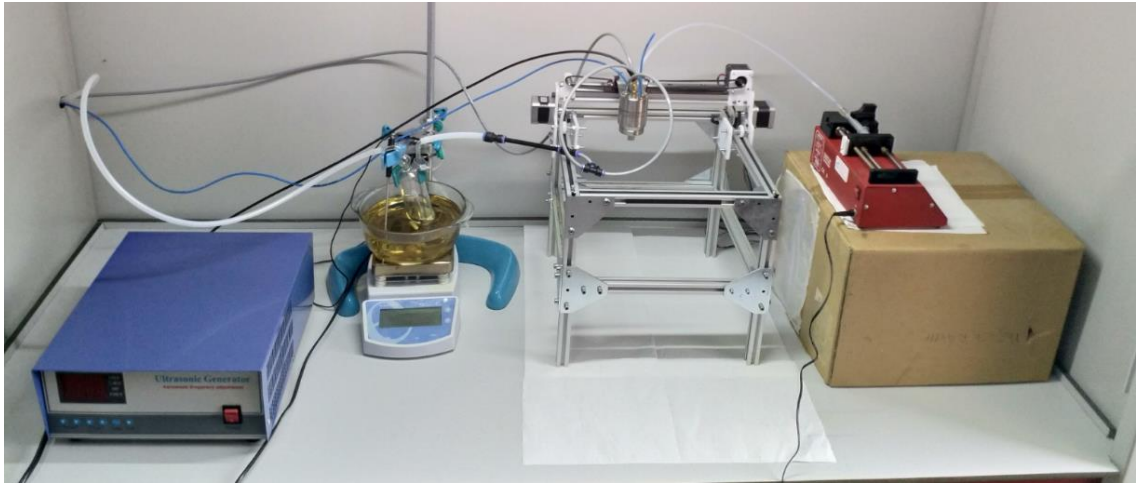
Figure 3. 5 The system of spray-cast perovskite deposition with antisolvent vapor.

CHAPTER 4

EXPERIMENTAL METHODS

In this section, how to make a perovskite solar cell step by step, and then characterization methods will be detailed.

4.1. Perovskite Solar Cell Fabrication

4.1.1 Etching

The first stage in device fabrication is chemical etching. Areas that are not to be etched on the FTO glasses (2.5cm*2.5cm) are masked with Kapton tape. Then, zinc powder is sprinkled over the area to be etched, and dilute HCl (hydrochloric acid) is poured on the powder. The FTO surface is negatively charged due to zinc electrons and begins to attract H_3O^+ ions. Hydrogen ions diffuse to tin oxide and break the bond between them. As a result of this reaction, FTO is etched. Etched FTOs are cleaned with a cotton swab dipped in deionized water, Kapton tapes are removed, and then FTOs are dried with a nitrogen gun.
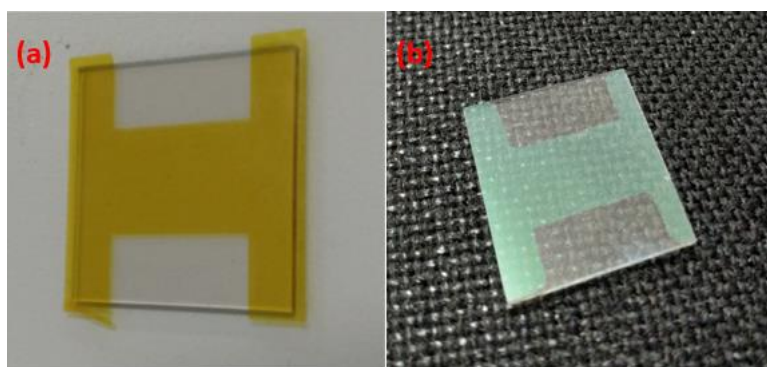
Figure 4. 1 Etching process, (a) a substrate masked with patterned Kapton tape (b) an etched substrate after the removal of the tape and subsequent cleaning.

4.1.2 Cleaning

Etched substrates are cleaned with detergent water, deionized water, and isopropanol for 10 minutes each, respectively. Each substrate is dried using a nitrogen gun. Then, substrates are placed in an oxygen plasma cleaner (10^{-2} mbar, 70 W) for 8 minutes to remove organic impurities from their surfaces.

4.1.3 Electron Transport Layer (ETL)

The c-TiO$_2$ solution is obtained by mixing titanium diisopropoxide bis (acetylacetonate) (TiDIP) and ethanol in a 1: 9 ratio. The m-TiO$_2$ solution is formed by diluting the titanic paste in 22% wt in ethanol.

ETL is coated by spin-coating on the cleaned substrates. Since we use a mesoporous structure, this process takes place in two steps. First, to form the c-TiO$_2$ layer, TiDIP solution is dropped onto the substrates on the spin coater and the substrate rotates at 3000 rpm for 30 seconds. The two edges of the coated substrate's etched region are cleaned with a cotton swab dipped in ethanol, which is the solvent of the TiDIP solution. The substrate is annealed at 500°C for 30 minutes.

The m-TiO$_2$ layer is coated on the c-TiO$_2$ coated substrates by spin-coating technique. The solution is cast on the substrate and the substrate begins to spin at 3000 rpm for 30 seconds. The two sides of the substrates with the etched region are cleaned with a swab dipped in ethanol, and the cleaned substrates are annealed at 550°C for 30 minutes.

4.1.4 Perovskite Layer

The perovskite precursor is obtained solution by mixing salts of 0.9 M MAI, 0.1 M MABr, 0.9 M PbI$_2$ and 0.1 M PbBr$_2$ in DMF: DMSO (4:1) at 60°C overnight.

MAPb(I$_{2.7}$ Br$_{0.3}$) precursor solution is sprayed onto the substrate with FTO / c-TiO2 / m-TiO2 layers at a temperature of the hot plate between 55-75°C. DMF is removed

during spraying. The films dry between 30 seconds and 60 seconds at the specified hot plate temperatures. After drying the precursor solution, the sample is annealed at 100 ℃ for 10 minutes. As a result of annealing, DMSO is removed from the film and the perovskite absorber layer is created. Next, the two FTO-etched edges of the substrate are again wiped with DMF and hold at 80 ℃ for a minute to remove DMF used for cleaning. As a result of these processes, we obtain samples as in Figure 4.2.
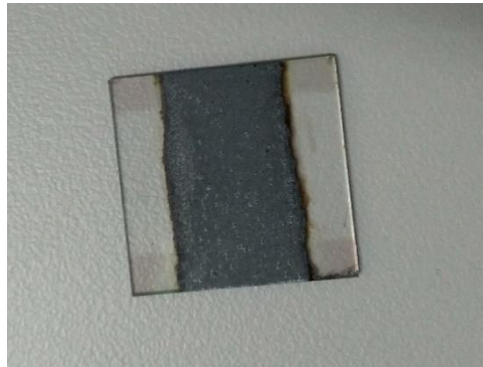
Figure 4. 2 Perovskite film with cleaned edges.

4.1.5 Hole Transport Layer (HTL)

For doped Spiro-OMeTAD, 180 mg Spiro-OMeTAD in 1 ml of chlorobenzene is mixed. Then, 37.5 µl of 170 mg LiTFSI (bis(trifluoromethanesulfonyl)imide), 1 ml Acetonitrile, and 18 µl TBP (4-tert-butyl-pyridine) mixture are added into Spiro-OMeTAD mixture. 20 µl of this resulting mixture is dripped onto the substrate in the spin coater and the substrate rotated at 4000 rpm for 30 seconds. Then, two sides of the substrate are wiped with chlorobenzene, the solvent of the mixture, and left to dry. The film should be kept under ambient conditions 6 hours for the Spiro-OMeTAD to oxidize and consequently increase its conductivity.

4.1.6 Gold Contact

The gold is coated on the samples by thermal evaporation. Substrates are placed on a substrate holder with a shadow mask. The sample holder is put on a rotating plate in the vacuum chamber and enough gold is added into a Tungsten boat to cover the desired

thickness. Then, the chamber is evacuated using a rough vacuum pump and a turbomolecular vacuum for proper metal deposition. When the pressure reaches below $4*10^{-6}$ mbar, the DC power is started to heat the Tungsten boat to reach the melting point of the gold in it. Since the chamber is kept at high vacuum, the gold begins to evaporate on the samples. Using a quartz crystal microbalance equipment, we track the evaporation rate of the gold and stop evaporation at the desired final thickness. The gold thickness should be at least 80 nm. We typically evaporated 100 nm gold at a rate of 0.03 nm/s for our p-metal contacts. As a result of evaporation, 4 devices are obtained on each sample as seen in Figure 4. 3.
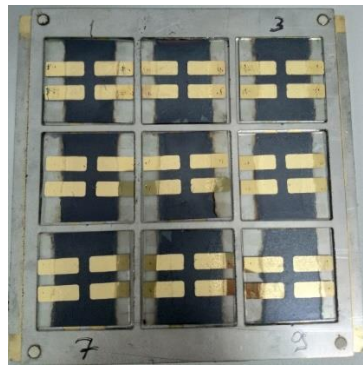
Figure 4. 3 The perovskite solar cells.

4.2. Characterization

In this section of Chapter 4, what methods are used to determine the properties of perovskite thin film and perovskite solar cell will be explained. The results from these methods will be discussed in Chapter 5.

4.2.1. Optical Microscopy

An optical microscope is a system using lenses that magnify images of objects. It uses visible light to perform this operation. It was used in our experiments to quickly detect major defects and inhomogeneities in films. The optical microscope allows us to get an idea of whether the film surface is homogeneous in a simple way.

4.2.2 Scanning Electron Microscopy (SEM)

Scanning electron microscopy provides high-resolution images from the film by using accelerated electrons instead of visible light. The sent electron beam hits atoms on the surface of the sample and stimulates secondary electrons. The signals from the emitted secondary electrons are detected by an electron detector and the morphological image of the surface is created. This process is carried out in a vacuum environment in order for the electron beam to reach the surface without hitting any gas molecules, hence to obtain a clear image from the sample.

SEM shows the crystals on the film and the continuity of the crystals on the nanometer scale. This allows us to obtain information about the homogeneity of the film and crystal growth.

Surface morphology images were taken from the Philips XL 30SFEG electron microscope.

4.2.3 X-Ray Diffraction (XRD)

By sending X-Ray rays on the sample, diffraction of the rays at specific angles is provided. By measuring the angles and intensities of these diffracted rays, information about the structure and size of the crystal grain, the positions of the atoms in the crystal, chemical bonds between atoms, and crystallographic disorders can be obtained.

Philips X'Pert Pro X-Ray Diffractometer was used for characterization. The step size for each film is $0.04°/s$ and XRD data were collected between $2\theta = 10°\text{-}50°$.

4.2.4 Current-Voltage Measurement

To measure the current-voltage graph, completed devices are fixed to between a printed circuit board (PCB) with pogo pins integrated and a specially designed slots (in accordance with our shadow mask design). This slot also acts as a shadow mask and has 4 squares spaces with an area of 0.16 cm^2 on it. The squares are exactly below the 4

devices on the sample. The pogo pin that touches the gold is connected to the anode and the pogo pin that touches the FTO is connected to the cathode. Then, the devices are subjected to AM 1.5 (1000 W/m^2) illumination by an Abet 11002 SunLite solar simulator, hence 4 active areas of 0.16 cm^2 are created in a sample. Current-voltage scans are obtained using a Keithley 2400 source meter shown in Figure 4. 5. To determine whether the device behaves like a typical pn-junction, measurements are taken in the dark. Then, the forward scan is performed from 0V to 1V and reverse scan from 1V to 0V at a speed of 0.4 V/s.
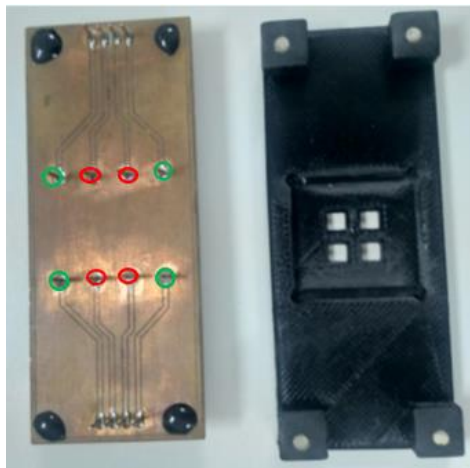
Figure 4. 4 The PCB and the slot which acts as a shadow mask. Red circles show pogo pins touched to gold and green circles show pogo pins touched FTO.
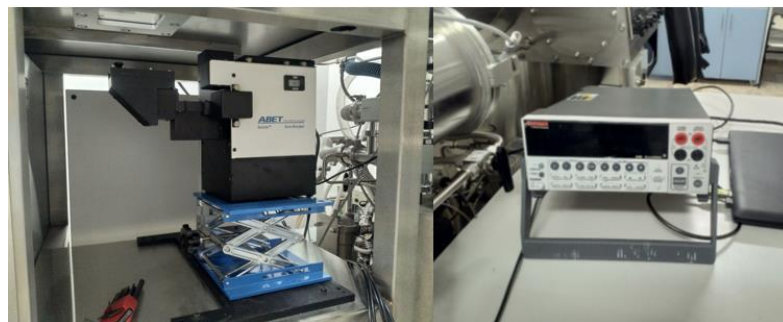
Figure 4. 5 Abet 11002 SunLite solar simulator and Keithley 2400 source meter.

CHAPTER 5

RESULTS AND DISCUSSION

5.1. Homogeneity of Perovskite Thin Films

Homogeneity is the first condition that must be met in order to produce high-quality films. Obtaining a homogeneous film has been the most time consuming and difficult procedure in this work. The prominent films obtained with various parameters tested throughout the process will be shared and the results are discussed.

Since our novel deposition system was newly set up, the spray had no movement system at first. It was not possible to create a homogeneous film with a stationary spray. Although a very small area in the middle of the film was homogeneous, there was major degradation in the remaining surface morphology. We observed that this was because the sprayed solution fell in the middle of the hot substrate and spread to the edges. Later, when we anneal the thin film, we noticed that visible morphological defects occurred.

The film seen in Figure 5.1 was obtained with the following parameters: Substrate temperature was 55°C, the distance between the nozzle and hot plate was 9 cm, the flow rate was 0.06 ml/min and spraying duration was 2 minutes.
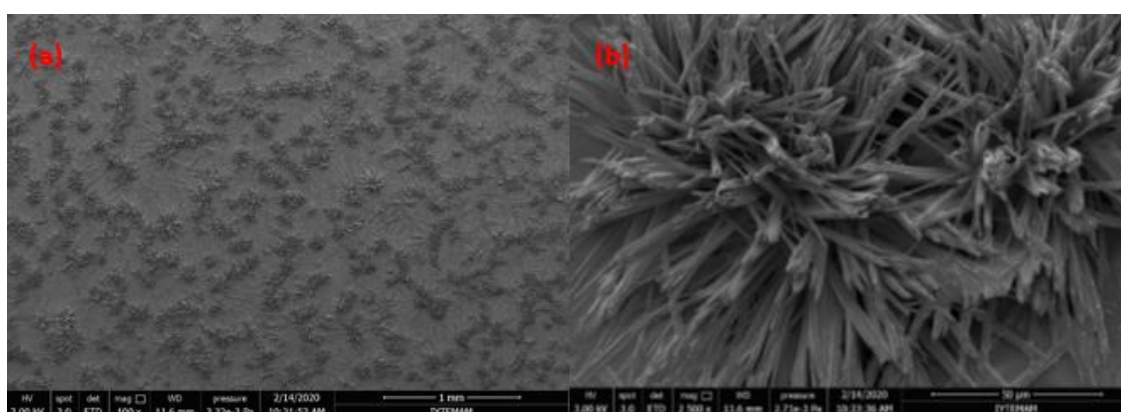
Figure 5. 1 (a) The morphology, (b) A defect of the film obtained by non-moving spray.

After the movement feature was added to the deposition system, double-pass spraying was tried. Although homogeneity increased slightly in these experiments, defects on the surface can still be noticed.

The parameters of the perovskite film obtained with the double pass spray seen in Figure 5.2 are as follows: Substrate temperature was 55 ℃, the distance between the nozzle and hot plate was 9 cm, the flow rate was 0.08 ml/min, and the spray moved on the x-axis at 20 mm/s.
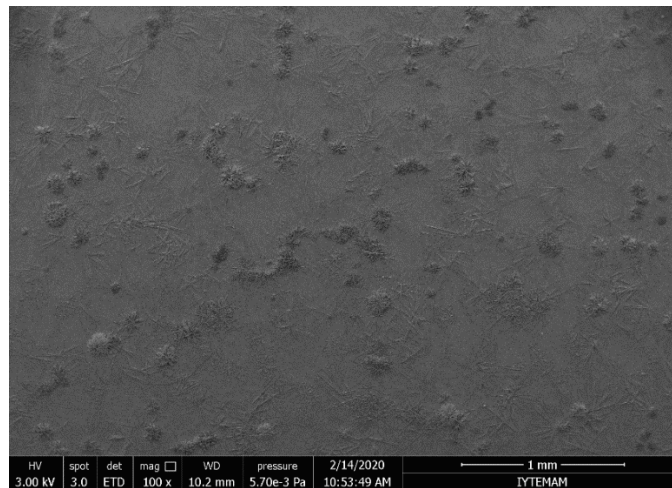
Figure 5. 2 The morphology of a film obtained by double-pass spraying.

Finally, we observed that the most homogeneous film that can be obtained by spray deposition can be achieved in one spray pass. Moreover, we learned that the flow rate and spray speed should be increased to increase the homogeneity.

We determined the optimum parameter values to reach the highest homogeneity that can be achieved as a result of the experiments. According to these results, the distance between hot plate and nozzle should be 9 cm, flow rate should be between 0.17 and 0.23 ml/min, spray speed should be between 70 and 100 mm/sec, substrate temperature should be between 60℃ and 75℃, and annealing should be done at 100℃ for 10 minutes.
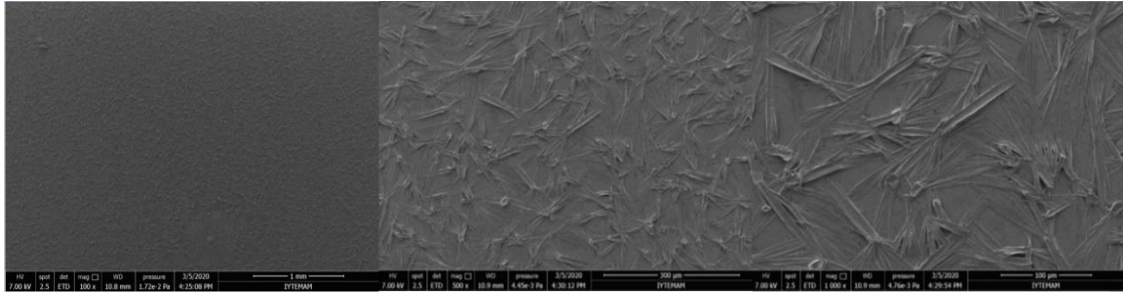
Figure 5. 3 A uniform morphology film obtained by single pass spraying.

5.2. Precursor Solution - Antisolvent Vapor Interaction

The interaction of solution and antisolvent is the most crucial point of this thesis. As it is known, antisolvent quenching method is used in spin coating. In spin coating, an antisolvent is left on the rotating solution to interact. The effect of antisolvent depends on dripping time and relative humidity (F. Wang et al. 2019). Antisolvent and perovskite solution interaction has not been realized in scalable deposition methods until now. We made this interaction with our novel system described in Chapter 3.

In the spray-cast deposition technique, the sprayed precursor solution begins to dry, when it falls onto hot substrate. Then, it changes from the δ-phase to the α-phase. In our deposition technique, an intermediate phase (red phase) occurs between the transition from δ-phase to α-phase thanks to DE vapor.

Figure 5. 4 The red phase and formation of a perovskite thin film.

The most important factor that determines the interaction is the substrate temperature in this novel deposition method. The red phase, which is only seen when using DE vapor, occurs when the substrate temperature is between 55 and 75°C.

When we used toluene vapor, the red phase was not seen, only the drying time of the film increased from 30 seconds to 1 minute. The use of DE vapor has no significant effect on the drying time. Antisolvent-free film and DE film dry in 30 seconds. We attribute the increase of drying time because of the difference between the boiling points of antisolvents.

We measured the power conversion efficiency (PCE) of our devices which have FTO/c-TiO2/m-TiO2/Perovskite/Spiro-OMeTAD/Au architecture. In different experiments, DE and TL vapor were sent to the precursor solution during spraying to see if the antisolvent vapor has an effect on the device efficiency. In addition, devices without antisolvent were produced to be the reference point. We made devices from produced films with uniform surfaces. We used an optical microscope to look at the morphology uniformity. In Figure 5.5, there are optical microscope images of a film with uniform surface morphology and a film with defective surface morphology.
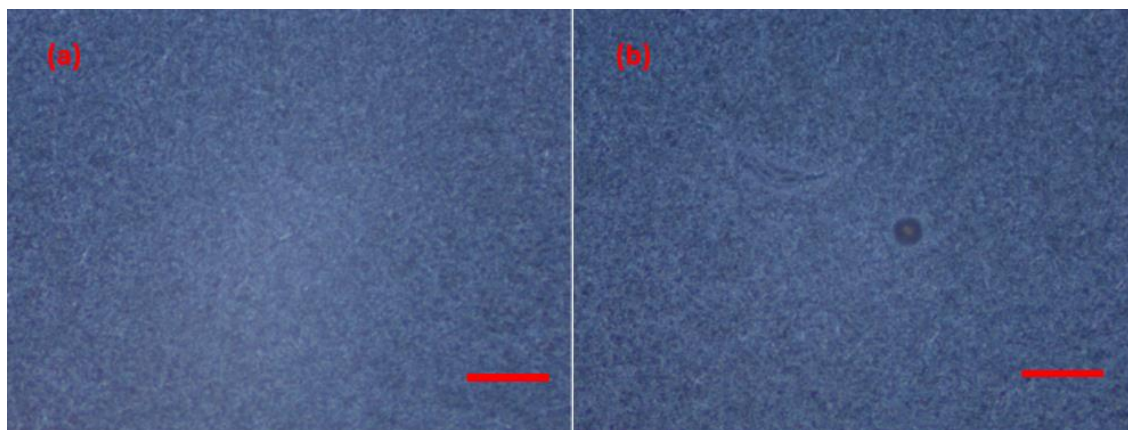
Figure 5. 5 Optical microscope images of perovskite thin films with (a) uniform surface morphology, (b) defective surface morphology. Red bars correspond to 200 μm.

The efficiency of the devices was low due to a problem in HTL process. We think that this problem is caused by materials that have lost their effect, or the shortness of oxidation time of spiro-OMeTAD. Despite the low efficiency, the devices were compared

among themselves as they went through the same processes. The results were noteworthy. The device with the highest efficiency was produced with DE vapor. The PCE of the device was 1.49%, FF was 0.32, V_{OC} was 0.78 V, and I_{SC} was 0.954 mA.
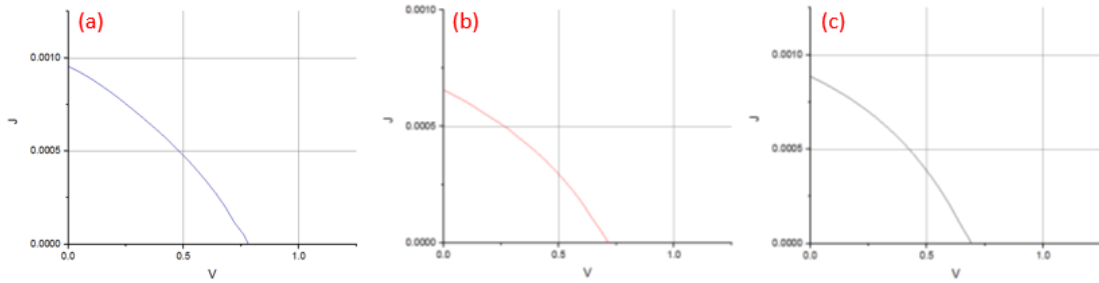
Figure 5. 6 J-V curves of the most efficient devices for (a) DE, (b) TL, (c) antisolvent-free.

Table 5. 1 The highest and average PCEs of devices produced with different antisolvents.

Antisolvent	Maximum PCE	Average PCE	Number of Devices
Diethyl Ether	%1.49	%1.24	5
Toluene	%0.98	%0.81	3
Antisolvent-free	%1.32	%1.03	5

Surprisingly, the devices with toluene have lower efficiency than their antisolvent-free counterparts. We think this is because toluene, which has a high boiling point, is condensed in the plastic tubing between the bubbler and the spray due to environmental conditions. Toluene, which comes as a liquid to the spray, mixes with the precursor solution. When the mixture falls on the substrate which has low temperature compared to the boiling point of toluene dries late. Our argument also explains why perovskite films with toluene dried late.

5.3. Crystallization

Crystallization is an important factor in understanding the quality of a perovskite thin film. The discontinuity of crystals in the film and pinholes between the crystal grains reduce the quality of the film. In this thesis, XRD data and SEM images are used to understand the characterization of the crystallization process.
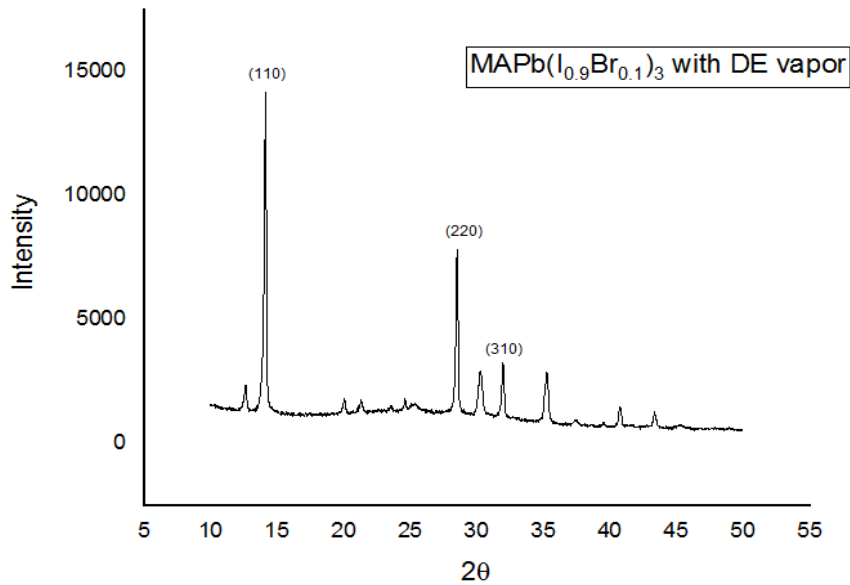
Figure 5. 7 XRD data of a perovskite thin film with DE.

The peaks formed in (110), (220), and (310) indicate that perovskite crystals are formed (Bai et al. 2017). The 2θ angles corresponding to these Miller indices are $14.13°$, $28.52°$, and $31.96°$, respectively. Based on this information, the perovskite crystals are successfully formed in our study.

The ratio of (110) and (310) peaks shows the effect of antisolvent on the crystal. The high rate means that crystallization is of high quality. This ratio was 2 in a study using spin-coating method, $MAPbI_3$ perovskite solution and DE as an antisolvent (Y. Li et al. 2017). In our study, the ratio was 4.37. We think that the reason for the high rate is that the perovskite solution we use contains Br.
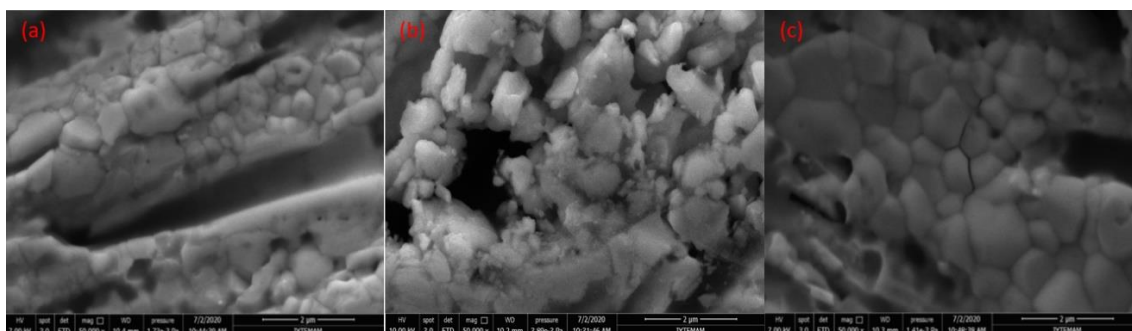
Figure 5. 8 SEM image of the crystal grains of, (a) DE, (b) TL, (c) without antisolvent.

As seen in SEM images, crystal formation is achieved in antisolvent-free and DE vapor films, while crystal formation in the toluene film appears to be defective. These images explain to us why the efficiency of toluene devices is low. In Figure 5.8 (a) and (b), the size of the crystals and less number of pin holes between them show that quality films can be produced in our system.

5.4. Further Development of Antisolvent Vapor-Assisted Spray Deposition System

The system has developed greatly since the first day it started operating. While the system needed more human intervention in the past, today it has become more automated. In this section of Chapter 5, to improve the system, the changes that can be made based on our observations will be discussed.

Reproducibility is a crucial factor for a device to be commercialized. There are some factors that prevent reproducibility for spray deposition such as ambient temperature and moisture. These factors should be kept under control by keeping it in a glovebox to increase repeatability.

The use of high boiling antisolvents in our system is difficult due to condensation in pipe between the bubbler and the spray. To overcome this problem, the pipe might be heated enough to prevent condensation.

Different antisolvent vapors can be mixed and dispatched the system to interact with the solution. In this way, better quality films can be created.

CHAPTER 6

CONCLUSIONS AND FUTURE WORK

The power conversion efficiencies (PCEs) of perovskite solar cells (PSCs) produced by scalable methods could not reach the PCEs of PSCs produced by spin-coating. Therefore, researches are carried out on increasing device efficiency by adding various novelties to scalable methods.

In this thesis, Antisolvent Vapor-Assisted Spray Deposition System is introduced. The production of antisolvent vapor and its integration into the spray-cast deposition method are detailed. The construction steps of perovskite solar cells are explained in detail, and information is given about which characterization methods are used. XRD data, power conversion efficiencies, optical microscope, and SEM images of the studies were shared the results were discussed. Ideas on how the system can be developed further were proposed.

As a result of these studies, the antisolvent quenching method was used successfully for the first time with a scalable deposition method. XRD data, PCE comparison, and intermediate phase formation are presented as proof of concept.

The device efficiencies in this study were lower than those in other spray deposition studies. It is thought that this is due to both the loss of effect of a material we use as HTL and our system, which is affected by environmental conditions. As a solution to this, we suggested that the spray deposition system be placed in a chamber that will not be affected by external influences.

Antisolvent Vapor-Assisted Spray Deposition System is a unique and successful method that can be included in other scalable systems. In slot-die coating, while spraying solution from a nozzle, nitrogen is given at high pressure to dry the solution with another head. The crystallization quality can be improved and the efficiency can be increased with an antisolvent-nitrogen mixture instead of nitrogen. Thus, a new step will be taken for the commercialization of perovskite solar cells.

REFERENCES

Ahn, Namyoung, Dae Yong Son, In Hyuk Jang, Seong Min Kang, Mansoo Choi, and Nam Gyu Park. 2015. "Highly Reproducible Perovskite Solar Cells with Average Efficiency of 18.3% and Best Efficiency of 19.7% Fabricated via Lewis Base Adduct of Lead(II) Iodide." *Journal of the American Chemical Society* 137 (27): 8696–99. https://doi.org/10.1021/jacs.5b04930.

Amokrane, G., C. Falentin-Daudré, S. Ramtani, and Véronique Migonney. 2018. "A Simple Method to Functionalize PCL Surface by Grafting Bioactive Polymers Using UV Irradiation." *Irbm* 39 (4): 268–78. https://doi.org/10.1016/j.irbm.2018.07.002.

Bai, Yang, Shuang Xiao, Chen Hu, Teng Zhang, Xiangyue Meng, Qiang Li, Yinglong Yang, Kam Sing Wong, Haining Chen, and Shihe Yang. 2017. "A Pure and Stable Intermediate Phase Is Key to Growing Aligned and Vertically Monolithic Perovskite Crystals for Efficient PIN Planar Perovskite Solar Cells with High Processibility and Stability." *Nano Energy* 34 (October 2016): 58–68. https://doi.org/10.1016/j.nanoen.2017.02.019.

Barrows, Alexander T., Andrew J. Pearson, Chan Kyu Kwak, Alan D.F. Dunbar, Alastair R. Buckley, and David G. Lidzey. 2014. "Efficient Planar Heterojunction Mixed-Halide Perovskite Solar Cells Deposited via Spray-Deposition." *Energy and Environmental Science*. https://doi.org/10.1039/c4ee01546k.

Behrouznejad, F., S. Shahbazi, N. Taghavinia, Hui Ping Wu, and Eric Wei-Guang Diau. 2016. "A Study on Utilizing Different Metals as the Back Contact of CH3NH3PbI3 Perovskite Solar Cells." *Journal of Materials Chemistry A* 4 (35): 13488–98. https://doi.org/10.1039/c6ta05938d.

Bishop, James E., David K. Mohamad, Michael Wong-Stringer, Alex Smith, and David G. Lidzey. 2017. "Spray-Cast Multilayer Perovskite Solar Cells with an Active-Area of 1.5 Cm2." *Scientific Reports* 7 (1): 1–11. https://doi.org/10.1038/s41598-017-08642-2.

Bishop, James E., Connor D. Read, Joel A. Smith, Thomas J. Routledge, and David G. Lidzey. 2020. "Fully Spray-Coated Triple-Cation Perovskite Solar Cells." *Scientific Reports* 10 (1): 1–8. https://doi.org/10.1038/s41598-020-63674-5.

Bishop, James E., Joel A. Smith, Claire Greenland, Vikas Kumar, Naoum Vaenas, Onkar S. Game, Thomas J. Routledge, Michael Wong-Stringer, Cornelia Rodenburg, and David G. Lidzey. 2018. "High-Efficiency Spray-Coated Perovskite Solar Cells Utilizing Vacuum-Assisted Solution Processing." *ACS Applied Materials and Interfaces* 10 (46): 39428–34. https://doi.org/10.1021/acsami.8b14859.

BPSTATS. 2019. "BP Statistical Review of World Energy Statistical Review of World, 68th Edition." *The Editor BP Statistical Review of World Energy*.

Bryant, Daniel, Nicholas Aristidou, Sebastian Pont, Irene Sanchez-Molina, Thana Chotchunangatchaval, Scot Wheeler, James R. Durrant, and Saif A. Haque. 2016. "Light and Oxygen Induced Degradation Limits the Operational Stability of Methylammonium Lead Triiodide Perovskite Solar Cells." *Energy and Environmental Science* 9 (5): 1655–60. https://doi.org/10.1039/c6ee00409a.

Cao, Duyen H., Constantinos C. Stoumpos, Omar K. Farha, Joseph T. Hupp, and Mercouri G. Kanatzidis. 2015. "2D Homologous Perovskites as Light-Absorbing Materials for Solar Cell Applications." *Journal of the American Chemical Society* 137 (24): 7843–50. https://doi.org/10.1021/jacs.5b03796.

Chapin, D. M., C. S. Fuller, and G. L. Pearson. 1954. "A New Silicon P-n Junction Photocell for Converting Solar Radiation into Electrical Power [3]." *Journal of Applied Physics* 25 (5): 676–77. https://doi.org/10.1063/1.1721711.

Chen, Wei Yi, Lin Long Deng, Si Min Dai, Xin Wang, Cheng Bo Tian, Xin Xing Zhan, Su Yuan Xie, Rong Bin Huang, and Lan Sun Zheng. 2015. "Low-Cost Solution-Processed Copper Iodide as an Alternative to PEDOT:PSS Hole Transport Layer for Efficient and Stable Inverted Planar Heterojunction Perovskite Solar Cells." *Journal of Materials Chemistry A* 3 (38): 19353–59. https://doi.org/10.1039/c5ta05286f.

Day, Joseph, S. Senthilarasu, and Tapas K. Mallick. 2019. "Improving Spectral Modification for Applications in Solar Cells: A Review." *Renewable Energy* 132: 186–205. https://doi.org/10.1016/j.renene.2018.07.101.

Dualeh, Amalie, Thomas Moehl, Nicolas Tétreault, Joël Teuscher, Peng Gao, Mohammad Khaja Nazeeruddin, and Michael Grätzel. 2014. "Impedance Spectroscopic Analysis of Lead Iodide Perovskite-Sensitized Solid-State Solar Cells." *ACS Nano* 8 (1): 362–73. https://doi.org/10.1021/nn404323g.

Dualeh, Amalie, Nicolas Tétreault, Thomas Moehl, Peng Gao, Mohammad Khaja Nazeeruddin, and Michael Grätzel. 2014. "Effect of Annealing Temperature on Film Morphology of Organic-Inorganic Hybrid Pervoskite Solid-State Solar Cells." *Advanced Functional Materials* 24 (21): 3250–58. https://doi.org/10.1002/adfm.201304022.

Eggers, Helge, Fabian Schackmar, Tobias Abzieher, Qing Sun, Uli Lemmer, Yana Vaynzof, Bryce S. Richards, Gerardo Hernandez-Sosa, and Ulrich W. Paetzold. 2020. "Inkjet-Printed Micrometer-Thick Perovskite Solar Cells with Large Columnar Grains." *Advanced Energy Materials* 10 (6). https://doi.org/10.1002/aenm.201903184.

Eperon, Giles E., Samuel D. Stranks, Christopher Menelaou, Michael B. Johnston, Laura M. Herz, and Henry J. Snaith. 2014. "Formamidinium Lead Trihalide: A Broadly Tunable Perovskite for Efficient Planar Heterojunction Solar Cells." *Energy and Environmental Science* 7 (3): 982–88. https://doi.org/10.1039/c3ee43822h.

Fang, Hong, and Puru Jena. 2016. "Super-Ion Inspired Colorful Hybrid Perovskite Solar Cells." *Journal of Materials Chemistry A*. https://doi.org/10.1039/c5ta09646d.

Fantacci, Simona, Filippo De Angelis, Mohammad K. Nazeeruddin, and Michael Grätzel. 2011. "Electronic and Optical Properties of the Spiro-MeOTAD Hole Conductor in Its Neutral and Oxidized Forms: A DFT/TDDFT Investigation." *Journal of Physical Chemistry C* 115 (46): 23126–33. https://doi.org/10.1021/jp207968b.

Fonash, Stephen J. 2010. *Solar Cell Device Physics*.

Friedlingstein, Pierre, Matthew W. Jones, Michael O'Sullivan, Robbie M. Andrew, Judith Hauck, Glen P. Peters, Wouter Peters, et al. 2019a. "Global Carbon Budget 2019." *Earth System Science Data* 11 (4): 1783–1838. https://doi.org/10.5194/essd-11-1783-2019.

———. 2019b. "Global Carbon Budget 2019." *Earth System Science Data*. https://doi.org/10.5194/essd-11-1783-2019.

Fu, Kunwu, Anita Wing Yi Ho-Baillie, Hemant Kumar Mulmudi, and Pham Thi Thu Trang. 2019. *Perovskite Solar Cells: Technology and Practices*. Apple Academic Press.

Gennes, P. G. De. 1985. "Wetting: Statics and Dynamics." *Reviews of Modern Physics* 57 (3): 827–63. https://doi.org/10.1103/RevModPhys.57.827.

Goetzberger, Adolf, and Volker U. Hoffmann. 2005. *Photovoltaic Solar Energy Generation. Photovoltaic Solar Energy Generation.* https://doi.org/10.1007/b137803.

Goldschmidt, V. M. 1926. "Die Gesetze Der Krystallochemie." *Die Naturwissenschaften.* https://doi.org/10.1007/BF01507527.

Heo, Jin Hyuck, Min Ho Lee, Min Hyeok Jang, and Sang Hyuk Im. 2016. "Highly Efficient CH3NH3PbI3−xClx Mixed Halide Perovskite Solar Cells Prepared by Re-Dissolution and Crystal Grain Growth via Spray Coating." *Journal of Materials Chemistry A* 4 (45): 17636–42. https://doi.org/10.1039/c6ta06718b.

Howard, Ian A., Tobias Abzieher, Ihteaz M. Hossain, Helge Eggers, Fabian Schackmar, Simon Ternes, Bryce S. Richards, Uli Lemmer, and Ulrich W. Paetzold. 2019. "Coated and Printed Perovskites for Photovoltaic Applications." *Advanced Materials* 31 (26). https://doi.org/10.1002/adma.201806702.

Huang, Haibo, Jiangjian Shi, Lifeng Zhu, Dongmei Li, Yanhong Luo, and Qingbo Meng. 2016. "Two-Step Ultrasonic Spray Deposition of CH3NH3PbI3 for Efficient and Large-Area Perovskite Solar Cell." *Nano Energy* 27: 352–58. https://doi.org/10.1016/j.nanoen.2016.07.026.

Hwang, Kyeongil, Yen Sook Jung, Youn Jung Heo, Fiona H. Scholes, Scott E. Watkins, Jegadesan Subbiah, David J. Jones, Dong Yu Kim, and Doojin Vak. 2015. "Toward Large Scale Roll-to-Roll Production of Fully Printed Perovskite Solar Cells." *Advanced Materials* 27 (7): 1241–47. https://doi.org/10.1002/adma.201404598.

"Inkjet Printing Process for Kesterite Solar Cells." n.d. Accessed June 29, 2020. https://www.helmholtz-berlin.de/pubbin/news_seite?nid=14203;sprache=en;seitenid=74699.

Ipcc. 2013. "Working Group I Contribution to the IPCC Fifth Assessment Report, Climate Change 2013: The Physical Science Basis." *Ipcc* AR5 (March 2013): 2014. http://ipccwg1.jp/AR4/meeting/pdf/SyR0407-siryo2.pdf.

Jang, Gyumin, Hyeok Chan Kwon, Sunihl Ma, Seong Cheol Yun, Hyunha Yang, and

Jooho Moon. 2019. "Cold Antisolvent Bathing Derived Highly Efficient Large-Area Perovskite Solar Cells." *Advanced Energy Materials* 9 (36): 1–13. https://doi.org/10.1002/aenm.201901719.

Jeon, Nam Joong, Jun Hong Noh, Young Chan Kim, Woon Seok Yang, Seungchan Ryu, and Sang Il Seok. 2014. "Solvent Engineering for High-Performance Inorganic-Organic Hybrid Perovskite Solar Cells." *Nature Materials* 13 (9): 897–903. https://doi.org/10.1038/nmat4014.

Jong, Un Gi, Chol Jun Yu, Jin Song Ri, Nam Hyok Kim, and Guk Chol Ri. 2016. "Influence of Halide Composition on the Structural, Electronic, and Optical Properties of Mixed CH3NH3Pb(I1-XBrx)3 Perovskites Calculated Using the Virtual Crystal Approximation Method." *Physical Review B* 94 (12): 1–8. https://doi.org/10.1103/PhysRevB.94.125139.

Kajal, Priyanka, Kunal Ghosh, and Satvasheel Powar. 2018. "Manufacturing Techniques of Perovskite Solar Cells," 341–64. https://doi.org/10.1007/978-981-10-7206-2_16.

Kim, Hui Seon, Chang Ryul Lee, Jeong Hyeok Im, Ki Beom Lee, Thomas Moehl, Arianna Marchioro, Soo Jin Moon, et al. 2012a. "Lead Iodide Perovskite Sensitized All-Solid-State Submicron Thin Film Mesoscopic Solar Cell with Efficiency Exceeding 9%." *Scientific Reports*. https://doi.org/10.1038/srep00591.

———. 2012b. "Lead Iodide Perovskite Sensitized All-Solid-State Submicron Thin Film Mesoscopic Solar Cell with Efficiency Exceeding 9%." *Scientific Reports* 2: 1–7. https://doi.org/10.1038/srep00591.

Kittel, Charles. 2004. "Introduction to Solid State Physics, 8th Edition." *Wiley & Sons, New York, NY*.

Kojima, Akihiro, Kenjiro Teshima, Yasuo Shirai, and Tsutomu Miyasaka. 2009. "Organometal Halide Perovskites as Visible-Light Sensitizers for Photovoltaic Cells." *Journal of the American Chemical Society*. https://doi.org/10.1021/ja809598r.

Konstantakou, Maria, Dorothea Perganti, Polycarpos Falaras, and Thomas Stergiopoulos. 2017. "Anti-Solvent Crystallization Strategies for Highly Efficient Perovskite Solar Cells." *Crystals* 7 (10): 1–21. https://doi.org/10.3390/cryst7100291.

Krishnamoorthy, Thirumal, Hong Ding, Chen Yan, Wei Lin Leong, Tom Baikie, Ziyi Zhang, Matthew Sherburne, et al. 2015. "Lead-Free Germanium Iodide Perovskite Materials for Photovoltaic Applications." *Journal of Materials Chemistry A*. https://doi.org/10.1039/c5ta05741h.

Lee, Da Seul, Jueming Bing, Jincheol Kim, Martin A. Green, Shujuan Huang, and Anita W.Y. Ho-Baillie. 2020. "Grain Quality Engineering for Organic Metal Halide Perovskites Using Mixed Antisolvent Spraying Treatment." *Solar RRL* 4 (1). https://doi.org/10.1002/solr.201900397.

Lee, Michael M., Joël Teuscher, Tsutomu Miyasaka, Takurou N. Murakami, and Henry J. Snaith. 2012. "Efficient Hybrid Solar Cells Based on Meso-Superstructured Organometal Halide Perovskites." *Science*. https://doi.org/10.1126/science.1228604.

Li, Yang, Jianan Wang, Yi Yuan, Xiandui Dong, and Peng Wang. 2017. "Anti-Solvent Dependent Device Performance in CH3NH3PbI3 Solar Cells: The Role of Intermediate Phase Content in the as-Prepared Thin Films." *Sustainable Energy and Fuels* 1 (5): 1041–48. https://doi.org/10.1039/c7se00125h.

Li, Zhen, Talysa R. Klein, Dong Hoe Kim, Mengjin Yang, Joseph J. Berry, Maikel F.A.M. Van Hest, and Kai Zhu. 2018. "Scalable Fabrication of Perovskite Solar Cells." *Nature Reviews Materials* 3: 1–20. https://doi.org/10.1038/natrevmats.2018.17.

Liu, Beibei, Shuo Wang, Zirui Ma, Jiawang Ma, Ruixin Ma, and Chengyan Wang. 2019. "High-Performance Perovskite Solar Cells with Large Grain-Size Obtained by the Synergy of Urea and Dimethyl Sulfoxide." *Applied Surface Science* 467–468: 708–14. https://doi.org/10.1016/j.apsusc.2018.10.141.

Liu, Mingzhen, Michael B. Johnston, and Henry J. Snaith. 2013. "Efficient Planar Heterojunction Perovskite Solar Cells by Vapour Deposition." *Nature* 501 (7467): 395–98. https://doi.org/10.1038/nature12509.

Meloni, Simone, Thomas Moehl, Wolfgang Tress, Marius Franckeviius, Michael Saliba, Yong Hui Lee, Peng Gao, et al. 2016. "Ionic Polarization-Induced Current-Voltage Hysteresis in CH3NH3PbX3 Perovskite Solar Cells." *Nature Communications* 7 (May 2015). https://doi.org/10.1038/ncomms10334.

Mirershadi, Soghra, Farhad Sattari, and Mahmoud Mohamadi Saridaragh. 2018. "Effects of Halogen Replacement on the Efficiency of Luminescent Solar Concentrator Based on Methylammonium Lead Halide Perovskite." *Solar Energy Materials and Solar Cells* 186 (March): 365–72. https://doi.org/10.1016/j.solmat.2018.07.008.

Mohamad, David K., Jonathon Griffin, Christopher Bracher, Alexander T. Barrows, and David G. Lidzey. 2016. "Spray-Cast Multilayer Organometal Perovskite Solar Cells Fabricated in Air." *Advanced Energy Materials* 6 (22): 1–7. https://doi.org/10.1002/aenm.201600994.

Mohamad Noh, Mohamad Firdaus, Chin Hoong Teh, Rusli Daik, Eng Liang Lim, Chi Chin Yap, Mohd Adib Ibrahim, Norasikin Ahmad Ludin, Abd Rashid Bin Mohd Yusoff, Jin Jang, and Mohd Asri Mat Teridi. 2018. "The Architecture of the Electron Transport Layer for a Perovskite Solar Cell." *Journal of Materials Chemistry C* 6 (4): 682–712. https://doi.org/10.1039/c7tc04649a.

Neamen, Donald A. 2006. *Semiconductor Physics and Devices Basic Principles*. *Materials Today*. Vol. 9. https://doi.org/10.1016/S1369-7021(06)71498-5.

Nelson, Jenny. 2003. *The Physics of Solar Cells*. *The Physics of Solar Cells*. https://doi.org/10.1142/p276.

Noel, Nakita K., Samuel D. Stranks, Antonio Abate, Christian Wehrenfennig, Simone Guarnera, Amir Abbas Haghighirad, Aditya Sadhanala, et al. 2014. "Lead-Free Organic-Inorganic Tin Halide Perovskites for Photovoltaic Applications." *Energy and Environmental Science* 7 (9): 3061–68. https://doi.org/10.1039/c4ee01076k.

Noman, M. A.A., M. J. Abden, and M. A. Islam. 2018. "Germanium Telluride Absorber Layer, A Proposal for Low Illumination Photovoltaic Application Using AMPS 1D." *International Conference on Computer, Communication, Chemical, Material and Electronic Engineering, IC4ME2 2018*, no. April. https://doi.org/10.1109/IC4ME2.2018.8465494.

NREL. 2019. "Best Research-Cell Efficiency Chart | Photovoltaic Research | NREL." *Best Research-Cell Efficiency Chart | Photovoltaic Research | NREL*.

Ortiz-Cervantes, Carmen, Paulina Carmona-Monroy, and Diego Solis-Ibarra. 2019. "Two-Dimensional Halide Perovskites in Solar Cells: 2D or Not 2D?" *ChemSusChem* 12 (8): 1560–75. https://doi.org/10.1002/cssc.201802992.

Paek, S., P. Schouwink, E. Nefeli Athanasopoulou, K. T. Cho, G. Grancini, Y. Lee, Y. Zhang, F. Stellacci, Mohammad Khaja Nazeeruddin, and P. Gao. 2017. "From Nano- to Micrometer Scale: The Role of Antisolvent Treatment on High Performance Perovskite Solar Cells." *Chemistry of Materials* 29 (8): 3490–98. https://doi.org/10.1021/acs.chemmater.6b05353.

Pellet, Norman, Peng Gao, Giuliano Gregori, Tae Youl Yang, Mohammad K. Nazeeruddin, Joachim Maier, and Michael Grätzel. 2014. "Mixed-Organic-Cation Perovskite Photovoltaics for Enhanced Solar-Light Harvesting." *Angewandte Chemie - International Edition* 53 (12): 3151–57. https://doi.org/10.1002/anie.201309361.

"Perovskites & Perovskite Solar Cell Structure, Efficiency and More | Ossila." n.d. Accessed June 29, 2020. https://www.ossila.com/pages/perovskites-and-perovskite-solar-cells-an-introduction.

Peters, G. P., R. M. Andrew, J. G. Canadell, P. Friedlingstein, R. B. Jackson, J. I. Korsbakken, C. Le Quéré, and A. Peregon. 2020. "Carbon Dioxide Emissions Continue to Grow amidst Slowly Emerging Climate Policies." *Nature Climate Change* 10 (1): 3–6. https://doi.org/10.1038/s41558-019-0659-6.

Qiu, Xiaofeng, Bingqiang Cao, Shuai Yuan, Xiangfeng Chen, Zhiwen Qiu, Yanan Jiang, Qian Ye, et al. 2017. "From Unstable CsSnI3 to Air-Stable Cs2SnI6: A Lead-Free Perovskite Solar Cell Light Absorber with Bandgap of 1.48 EV and High Absorption Coefficient." *Solar Energy Materials and Solar Cells* 159: 227–34. https://doi.org/10.1016/j.solmat.2016.09.022.

Rapier, Roberts. 2019. "Renewables Catching Nuclear Power In Global Energy Race." Forbes. 2019. https://www.forbes.com/sites/rrapier/2019/07/07/wind-and-solar-power-nearly-matched-nuclear-power-in-2018/#750eec4f39ee.

Rong, Yaoguang, Yue Ming, Wenxian Ji, Da Li, Anyi Mei, Yue Hu, and Hongwei Han. 2018. "Toward Industrial-Scale Production of Perovskite Solar Cells: Screen Printing, Slot-Die Coating, and Emerging Techniques." *Journal of Physical Chemistry Letters* 9 (10): 2707–13. https://doi.org/10.1021/acs.jpclett.8b00912.

Rose, Gustav. 1840. "Beschreibung Einiger Neuen Mineralien Des Urals." *Annalen Der Physik* 126 (8): 652–56. https://doi.org/10.1002/andp.18401260807.

Saliba, Michael, Juan Pablo Correa-Baena, Michael Grätzel, Anders Hagfeldt, and Antonio Abate. 2018. "Perovskite Solar Cells: From the Atomic Level to Film Quality and Device Performance." *Angewandte Chemie - International Edition* 57 (10): 2554–69. https://doi.org/10.1002/anie.201703226.

Saliba, Michael, Taisuke Matsui, Konrad Domanski, Ji Youn Seo, Amita Ummadisingu, Shaik M. Zakeeruddin, Juan Pablo Correa-Baena, et al. 2016. "Incorporation of Rubidium Cations into Perovskite Solar Cells Improves Photovoltaic Performance." *Science*. https://doi.org/10.1126/science.aah5557.

Saliba, Michael, Taisuke Matsui, Ji Youn Seo, Konrad Domanski, Juan Pablo Correa-Baena, Mohammad Khaja Nazeeruddin, Shaik M. Zakeeruddin, et al. 2016. "Cesium-Containing Triple Cation Perovskite Solar Cells: Improved Stability, Reproducibility and High Efficiency." *Energy and Environmental Science* 9 (6): 1989–97. https://doi.org/10.1039/c5ee03874j.

Shockley, William, and Hans J. Queisser. 1961. "Detailed Balance Limit of Efficiency of P-n Junction Solar Cells." *Journal of Applied Physics* 32 (3): 510–19. https://doi.org/10.1063/1.1736034.

Smith, Zachary A, and Katrina D Taylor. 2008. *Renewable and Alternative Energy: Resources: A Reference Handbook*.

Snaith, Henry J., Antonio Abate, James M. Ball, Giles E. Eperon, Tomas Leijtens, Nakita K. Noel, Samuel D. Stranks, Jacob Tse Wei Wang, Konrad Wojciechowski, and Wei Zhang. 2014. "Anomalous Hysteresis in Perovskite Solar Cells." *Journal of Physical Chemistry Letters* 5 (9): 1511–15. https://doi.org/10.1021/jz500113x.

Sze, S. M. 1985. *Semiconductor Devices - Physics and Technology*.

———. 2002. *Semiconductor Devices - Physics and Technology*. *John Wiley & Sons, Inc.* Vol. 23. https://doi.org/10.1177/002072098602300117.

Wang, Dian, Matthew Wright, Naveen Kumar Elumalai, and Ashraf Uddin. 2016. "Stability of Perovskite Solar Cells." *Solar Energy Materials and Solar Cells* 147: 255–75. https://doi.org/10.1016/j.solmat.2015.12.025.

Wang, Feng, Ting Zhang, Yafei Wang, Detao Liu, Peng Zhang, Hao Chen, Long Ji, et al. 2019. "Steering the Crystallization of Perovskites for High-Performance Solar Cells

in Ambient Air." *Journal of Materials Chemistry A* 7 (19): 12166–75. https://doi.org/10.1039/c9ta02566a.

Whitaker, James B., Dong Hoe Kim, Bryon W. Larson, Fei Zhang, Joseph J. Berry, Maikel F.A.M. Van Hest, and Kai Zhu. 2018. "Scalable Slot-Die Coating of High Performance Perovskite Solar Cells." *Sustainable Energy and Fuels* 2 (11): 2442–49. https://doi.org/10.1039/c8se00368h.

Wu, Wu Qiang, Qi Wang, Yanjun Fang, Yuchuan Shao, Shi Tang, Yehao Deng, Haidong Lu, et al. 2018. "Molecular Doping Enabled Scalable Blading of Efficient Hole-Transport-Layer-Free Perovskite Solar Cells." *Nature Communications* 9 (1): 1–8. https://doi.org/10.1038/s41467-018-04028-8.

Xiao, Manda, Fuzhi Huang, Wenchao Huang, Yasmina Dkhissi, Ye Zhu, Joanne Etheridge, Angus Gray-Weale, Udo Bach, Yi Bing Cheng, and Leone Spiccia. 2014. "A Fast Deposition-Crystallization Procedure for Highly Efficient Lead Iodide Perovskite Thin-Film Solar Cells." *Angewandte Chemie - International Edition* 53 (37): 9898–9903. https://doi.org/10.1002/anie.201405334.

Yang, Woon Seok, Jun Hong Noh, Nam Joong Jeon, Young Chan Kim, Seungchan Ryu, Jangwon Seo, and Sang Il Seok. 2015. "High-Performance Photovoltaic Perovskite Layers Fabricated through Intramolecular Exchange." *Science* 348 (6240): 1234–37. https://doi.org/10.1126/science.aaa9272.

Zhang, Qi, Feng Hao, Jianbao Li, Yangying Zhou, Yaxuan Wei, and Hong Lin. 2018. "Perovskite Solar Cells: Must Lead Be Replaced–and Can It Be Done?" *Science and Technology of Advanced Materials* 19 (1): 425–42. https://doi.org/10.1080/14686996.2018.1460176.

Zheng, Xiaojia, Congcong Wu, Shikhar K. Jha, Zhen Li, Kai Zhu, and Shashank Priya. 2016. "Improved Phase Stability of Formamidinium Lead Triiodide Perovskite by Strain Relaxation." *ACS Energy Letters* 1 (5): 1014–20. https://doi.org/10.1021/acsenergylett.6b00457.

Zhou, Xianyong, Yong Zhang, Weiguang Kong, Manman Hu, Luozheng Zhang, Chang Liu, Xiangnan Li, et al. 2018. "Crystallization Manipulation and Morphology Evolution for Highly Efficient Perovskite Solar Cell Fabrication: Via Hydration Water Induced Intermediate Phase Formation under Heat Assisted Spin-Coating."

Journal of Materials Chemistry A 6 (7): 3012–21. https://doi.org/10.1039/c7ta08947c.

Zhou, Yuanyuan, Onkar S. Game, Shuping Pang, and Nitin P. Padture. 2015. "Microstructures of Organometal Trihalide Perovskites for Solar Cells: Their Evolution from Solutions and Characterization." *Journal of Physical Chemistry Letters* 6 (23): 4827–39. https://doi.org/10.1021/acs.jpclett.5b01843.

Zhou, Yuanyuan, Mengjin Yang, Onkar S. Game, Wenwen Wu, Joonsuh Kwun, Martin A. Strauss, Yanfa Yan, Jinsong Huang, Kai Zhu, and Nitin P. Padture. 2016. "Manipulating Crystallization of Organolead Mixed-Halide Thin Films in Antisolvent Baths for Wide-Bandgap Perovskite Solar Cells." *ACS Applied Materials and Interfaces* 8 (3): 2232–37. https://doi.org/10.1021/acsami.5b10987.